MICROCOPY RESOLUTION TEST CHART

NATIONAL BUREAU OF STANDARDS-1963-A

AD A138392

(12)

155900-15-T

Topic Report

MEASUREMENT OF OCEAN SURFACE WINDS BY SEASAT SYNTHETIC APERTURE RADAR

J.D. LYDEN
D.R. LYZENGA
R.A. SHUCHMAN

Radar Division

W.L. JONES

National Aeronautics and Space Administration
Langley Research Center
Hampton, VA 23665

JULY 1983

DTIC
SELECTED
FEB 2 4 1984
E

DTIC FILE COPY

∑ ENVIRONMENTAL
RESEARCH INSTITUTE OF MICHIGAN
BOX 8618 ● ANN ARBOR ● MICHIGAN 48107

84 02 23 011

SECURITY CLASSIFICATION OF THIS PAGE *(When Data Entered)*

REPORT DOCUMENTATION PAGE		READ INSTRUCTIONS BEFORE COMPLETING FORM
1. REPORT NUMBER	2. GOVT ACCESSION NO. AD-A138392	3. RECIPIENT'S CATALOG NUMBER
4. TITLE *(and Subtitle)* MEASUREMENT OF OCEAN SURFACE WINDS BY SEASAT SYNTHETIC APERTURE RADAR		5. TYPE OF REPORT & PERIOD COVERED Topic Report
		6. PERFORMING ORG. REPORT NUMBER 155900-15-T
7. AUTHOR(s) J.D. Lyden, D.R. Lyzenga, R.A. Shuchman, and W.L. Jones		8. CONTRACT OR GRANT NUMBER(s) N00014-81-C-0692
9. PERFORMING ORGANIZATION NAME AND ADDRESS Environmental Research Institute of Michigan Radar Division, P.O. Box 8618, Ann Arbor, Michigan 48107		10. PROGRAM ELEMENT, PROJECT, TASK AREA & WORK UNIT NUMBERS
11. CONTROLLING OFFICE NAME AND ADDRESS Ocean Sciences Division Office of Naval Research Arlington, VA 22217		12. REPORT DATE July 1983
		13. NUMBER OF PAGES xiv + 96
14. MONITORING AGENCY NAME AND ADDRESS *(if different from Controlling Office)*		15. SECURITY CLASS. *(of this report)* Unclassified
		15a. DECLASSIFICATION/DOWNGRADING SCHEDULE

16. DISTRIBUTION STATEMENT *(of this Report)*

Approved for public release; distribution unlimited.

17. DISTRIBUTION STATEMENT *(of the abstract entered in Block 20, if different from Report)*

18. SUPPLEMENTARY NOTES

The technical monitors for this work were Mr. Hans Dolezalek and Commander Robert Kirk. W.L. Jones now with Satellite Television Corp., Princeton Junction, NJ 08550.

19. KEY WORDS *(Continue on reverse side if necessary and identify by block number)*

Synthetic Aperture Radar
Seasat   Optical Processing
Wind Measurements
Doppler Spectrum Shifting

20. ABSTRACT *(Continue on reverse side if necessary and identify by block number)*

This report investigates the feasibility of using Seasat Synthetic Aperture Radar (SAR) data for measuring ocean surface winds. An empirical model relating the received power of the L-band SAR to ocean surface wind conditions was evaluated. Results from this investigation indicate that past Seasat SAR wind studies could be biased due to the nature of the measurement techniques employed. In these past studies, densitometer measurements of output imagery were related to wind speed and direction. Because of a shifting

DD , FORM JAN 73 1473   EDITION OF 1 NOV 65 IS OBSOLETE

SECURITY CLASSIFICATION OF THIS PAGE *(When Data Entered)*

20. ABSTRACT (Continued)

of the Doppler spectrum location with latitude due to the earth's rota-
tion and spacecraft attitude changes, these measurements are valid only
over short azimuthal distances. A theoretical correction was calculated
and applied to the Seasat data, resulting in improved correlations with
the surface wind speed. Additionally, a simplified measurement technique
which did not involve explicit corrections for this Doppler shifting was
developed. The results of this study are consistent with those of pre-
vious investigations, but yield additional insight into the angular
dependence of the SAR backscatter and the accuracy of the technique.

PREFACE

The work described in this report was conducted by the Radar Division of the Environmental Research Institute of Michigan (ERIM). The work was supported by the Office of Naval Research (ONR) Contract No. N-00014-81-C-0682. The technical monitors for this work were Mr. Hans Dolezalek and Commander Robert Kirk.

The Principal Investigator for this contract is Dr. Robert A. Shuchman. Mr. James D. Lyden performed the comparison of SASS winds and SAR measurements. Dr. David R. Lyzenga contributed the work on Doppler spectrum shifting as well as the theoretical scattering model results. Dr. W. Linwood Jones provided the SASS data while at NASA Langley Research Center.

Accession For		
NTIS GRA&I	☑	
DTIC TAB	☐	
Unannounced	☐	
Justification		
By		
Distribution/		
Availability Codes		
Dist	Avail and/or Special	
A-1		

iii

ACKNOWLEDGMENTS

TABLE OF CONTENTS

LIST OF FIGURES

LIST OF FIGURES (CONTINUED)

LIST OF FIGURES (CONTINUED)

LIST OF FIGURES (CONCLUDED)

LIST OF TABLES

1
INTRODUCTION

The purpose of this study was to evaluate the ability of the synthetic aperture radar (SAR) aboard Seasat to provide ocean surface wind information. This study evaluated an empirical relationship between the Seasat SAR data and ocean surface wind speed and direction. Specifically, the Seasat SAR observed radar backscatter from the ocean surface was corrected for system effects and then statistically compared to the Seasat scatterometer (SASS) derived surface winds. The results of this analysis agree in general with those of previous investigators, but lend additional insight into the angular dependence of the SAR backscatter and the accuracy of the technique.

Knowledge of ocean surface winds on the synoptic scale is of great importance to a wide range of ocean-related activities including: short-range weather predictions, ship routing, commercial fishing, and offshore mining and energy exploration activities. Much of the importance is because ocean surface gravity waves are the result of wind interacting with the ocean surface. Knowledge of the wind characteristics (speed, direction, and duration) in a wave generation area allows for prediction of future wave characteristics, hundreds or even thousands of kilometers away. The economic importance of such predictions are obvious.

Current knowledge of the ocean surface wind field is limited to a collection of coarsely sampled (both spatially and temporally) surface observations. The sampling requirements necessary for useful wind data (wave predictions) would require a monumental, if not impossible, surface-based measurement effort. Clearly, the most feasible and cost-effective method of acquiring wind data is through the use of remote sensors operating from spaceborne platforms.

This report documents the results of a study on the use of Seasat
SAR data for measuring ocean surface winds. It consists of a back-
ground section which includes discussions on the theory of microwave
measurements of ocean surface roughness, a review of past studies
using Seasat SAR data to measure ocean surface winds, and a review
of the Seasat SAR system characteristics with particular emphasis on
special considerations that must be made when using the data for wind
measurements. This is followed by a section which describes the data
set and measurement techniques used in this study. The next section
presents our analysis and results, which include the evaluation of
an empirical model for relating the SAR-observed backscatter to the
ocean surface wind field. Additionally, a comparison of our model
results with those predicted by a theoretical scattering model is
presented. Finally, conclusions and recommendations are presented.

2
BACKGROUND

Presented in this section is a brief review of the theory of microwave measurements of ocean surface roughness, and a review of past studies using scatterometer and Seasat synthetic aperture radar (SAR) data to measure ocean surface winds. In addition, a review of the Seasat SAR system characteristics is presented with particular emphasis on special considerations that must be made when using the data for wind measurements.

2.1 SAR DETECTION OF OCEAN SURFACE ROUGHNESS

The basic assumption of using any microwave instrument for ocean surface wind measurements is that there is a relationship between the amount of energy received by the instrument and the ocean surface roughness. For active microwave instruments such as a SAR, the amount of energy received from the ocean surface increases with in-creasing surface roughness. Surface measurements of waves have led to empirical relationships between wave characteristics and wind speed and direction. Therefore, the problem becomes one of relating the SAR measurements to wind data via an appropriate scattering model.

Several scattering models exist that attempt to explain ocean surface image formation with synthetic aperture radars. These models are of two types: static models that depend on instantaneous surface features, and dynamic models that employ surface scatterer veloc-ities. Considerable debate exists on the limitations and applicabil-ity of either model.

Several static models have been suggested to describe the radar scattering of energy from large areas on the ocean surface. These scattering models include: (1) the tangent-plane or quasi-specular model which is most appropriate for small incidence angles, (2) the

3

Bragg-Rice scattering model, which assumes small deviations from a planar surface and correlates well with experimental data for incidence angles larger than 10°, and (3) wedge and Rayleigh scattering models which attempt to account for surface elements which have small radii of curvature relative to the radar wavelength. There is a general consensus within the radio-oceanography scientific community that a Bragg-Rice scattering theory best explained the Seasat SAR observed backscatter values obtained from the ocean surface. The Bragg-Rice scattering model is based on a well known phenomena in the study of crystals, gratings, and periodic structures. If one considers the random ocean surface to be represented by a combination of periodic surfaces (i.e., a spectrum), then the spectrum region which satisfies the backscatter phase matching condition will be the main contributor to the backscatter cross section. Under higher wind conditions, however, wedge scattering may also be important, particularly for larger incidence angles and shorter radar wavelengths (Lyzenga, et al., 1983).

Pioneering theoretical and experimental work by Wright (1966) at the Naval Research Laboratory (NRL) demonstrated the general validity of a Bragg scattering model for an ocean surface imaged by radar. In a series of wave tank measurements using 3 and 25 cm wavelength continuous wave (CW) Doppler radars, Wright (1966) demonstrated Bragg scattering. That is, transmitted radar energy with wave number K interacts in a resonant or constructive interference fashion with ocean surface waves of wave number K_W such that

$$K_W = 2K \sin \theta, \tag{1}$$

where $K_W = 2\pi/L$ and $K = 2\pi/\lambda$, L and λ are the wavelengths of the surface waves and the radar, respectively, and θ is the incidence angle. Shuchman, et al. (1981) showed that Bragg scattering satisfactorily explained the radar backscatter return for SAR data

4

collected during the Marineland experiment. It should be noted that radar data of large ocean areas (1 x 1 km) were averaged in that analysis and the wind speed was approximately 7 m/s.

Scatterer motions cause two effects in SAR imagery: first, they cause a displacement of the scatterers in the azimuth direction (the "train-off-the-track" effect) by an amount proportional to the radial velocity of the scatterers, and second, they may cause some attenuation of the signals due to Doppler shifting out of the passband of the SAR receiver/recorder or the processor. In Seasat data, a significant radial velocity is imparted to the scatterers by the earth's rotation beneath the spacecraft orbit. This radial velocity causes some geometric distortion of the SAR images due to the displacement effect mentioned above, but the distortion is not crucial to the analyses presented in this report. The signal attenuation due to Doppler shifting is an important effect, however, as described and accounted for later in this report. Scatterer velocities due to ocean waves produce differential displacements which may be important for understanding the fine structure of the imagery, but these displacements are much smaller than the spatial scales considered in this study and therefore do not affect these results.

2.2 PAST SCATTEROMETER AND SEASAT SAR WIND STUDIES

Several studies have been performed over the past few years concerning the use of microwave radar for measuring ocean surface winds (Jones, et al., 1979; Jones and Schroeder, 1978; Thompson, et al., 1981). These studies have typically assumed an empirical model of the form

$$\sigma_0 = U^\gamma (1 + \alpha_1 \cos \psi + \alpha_2 \cos 2\psi) , \qquad (2)$$

where σ_0 is the normalized radar cross section, U is the wind speed, γ is the wind speed exponent, α_1 and α_2 are anisotropy coefficients, and ψ is the radar line-of-sight relative to upwind.

The validity of this model for radar/wind studies was first demonstrated with data collected by a K_u-band (2.2 cm wavelength) airborne scatterometer as described by Jones, et al. (1977). During this experiment, measurements were made from an aircraft flown in a series of 360° turns. This flight pattern allowed for the measurement of the anisotropic scattering characteristics of the wind-roughened ocean surface. These results are shown in Figure 1 for like-polarized (horizontal-transmit, horizontal-receive) data collected at three wind speeds. The normalized radar cross section behaves nearly sinusoidally at high wind speeds and becomes more uniform with decreasing wind speed. The normalized radar cross section is seen to peak in the upwind and downwind directions and are minimum in the crosswind direction. This is accounted for in Eq. (2) by the a_2 anisotropy coefficient. Additionally, the upwind peak is slightly larger than the downwind peak. This is accounted for in Eq. (2) by the a_1 anisotropy coefficient.

The highly anisotropic behavior of ocean surface backscatter at Ku-band has never been demonstrated at L-band for moderate wind conditions. A study by Jones and Schroeder (1978) of L-band scatterometer data collected by the Naval Research Laboratory (NRL) at 30° incidence angle (Daley, 1973), indicated very little anisotropic behavior. Their results are shown plotted in Figure 2 for a variety of radar frequencies. The points on this graph represent the upwind-to-crosswind and upwind-to-downwind, backscatter ratios. For L-band (23.5 cm wavelength) these are both seen to be less than 1 dB. This study, as well as others in the past, is an attempt to quantify the isotropic/anisotropic qualities of Seasat SAR L-band data using the above model.

During the Duck, N.C. Experiment (Duck-X), the Seasat SAR collected data during Revolution 1339. These data were studied by Beal (1979) and Jones, et al. (1981). Both studies utilized densitometer measurements of image film which were later calibrated following the procedure outlined by Huneycutt (1979). In his study, Beal compared

6

SCATTEROMETER MEASUREMENTS
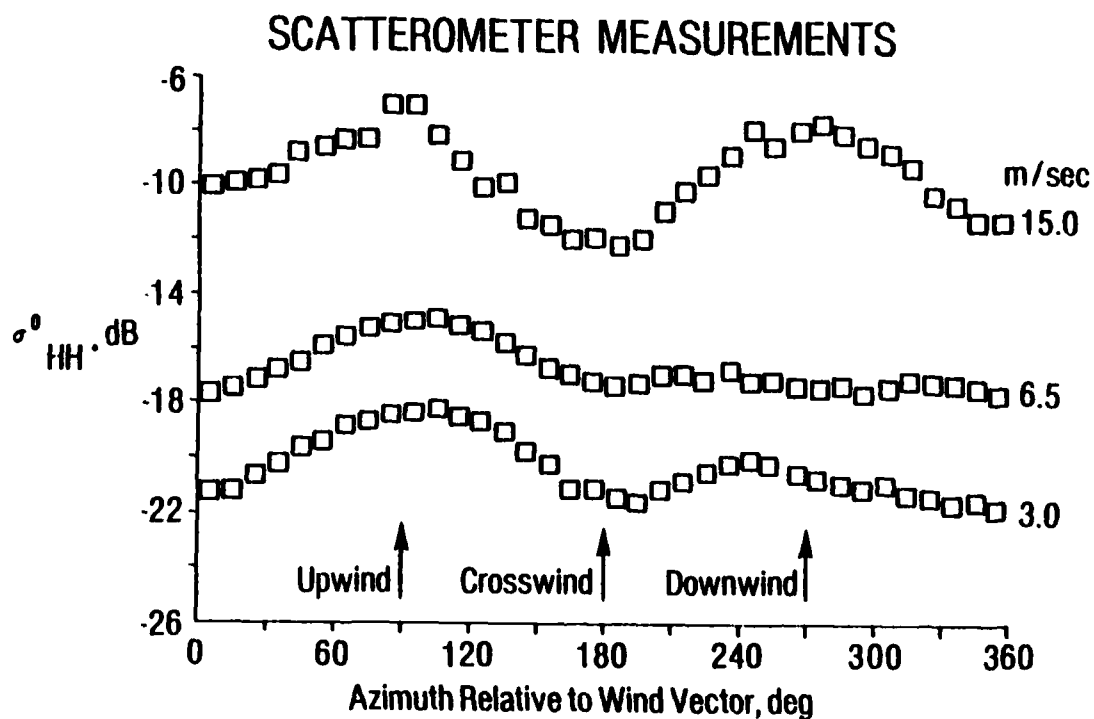
Figure 1. Anisotropic Scattering Characteristics of 13.9 GHz Like-Polarized (HH) Scatterometer Data at 30° Incidence Angle (After Jones, et al., 1977)
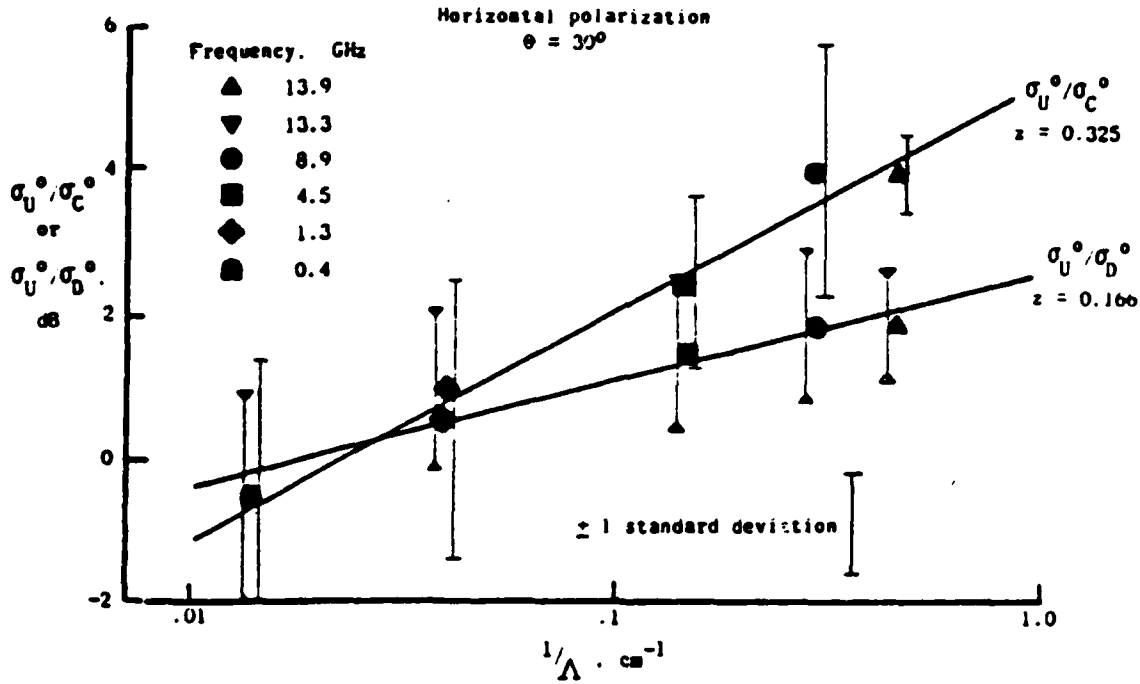
Figure 2.   Upwind-to-Crosswind ($6\sigma_U°/\sigma_C°$) and Upwind-to-Downwind ($\sigma_U°/\sigma_D°$) Cross Section Ratios vs. Reciprocal Bragg Wavelength for Like-Polarized Scatterometer Data at 30° Incidence Angle (After Jones and Schroeder, 1978)

these SAR data to coincident wind measurements made by the Seasat scatterometer (SASS) using Eq. (2), but with the added assumption that a simple power law relationship was valid (i.e., $\alpha_1 = \alpha_2 = 0$). These measurements are shown in Figure 3. He concluded that for this data set, a wind speed exponent between 0.5 and 0.65 produced the best results.

The Jones study compared the SAR data to coincident wind measurements made by the SASS and the Seasat underflight scatterometer (SUS) flown on a C-130 aircraft. Employing Eq. (2) and ignoring the upwind/downwind anisotropy (i.e., $\alpha_1 = 0$), a wind speed exponent (γ) of 0.4 and an upwind/crosswind anisotropy coefficient (α_2) of 0.02 were found to give the best results. These parameters were then used to infer wind speeds at additional locations for comparison with the SASS. The results of this comparison are shown in Figure 4.

An interesting feature of the above two studies is the apparent lack of agreement between the wind speed exponent obtained by Beal (0.5-0.65) and Jones (0.4). This could be due in part to the inclusion of upwind/crosswind anisotropic effects by Jones, but is not likely due to the negligible value for α_2 he found (0.02). A more likely explanation for the discrepancy in wind speed exponent values is due to the method of deriving normalized radar cross section values from densitometer measurements of image film.

One other study which related Seasat SAR data to SASS-inferred winds using Eq. (2) was performed by Thompson, et al. (1981). These data were collected during the Gulf of Alaska Seasat Experiment (GOASEX). This study also used the method of Huneycutt to derive radar cross section from image film densities. This study averaged these cross section measurements for all four quarter swaths to obtain one value at each azimuth location. An example of these measurements, as well as the SASS-inferred winds for three revolutions are shown plotted in Figure 5. In their analysis, they assumed that
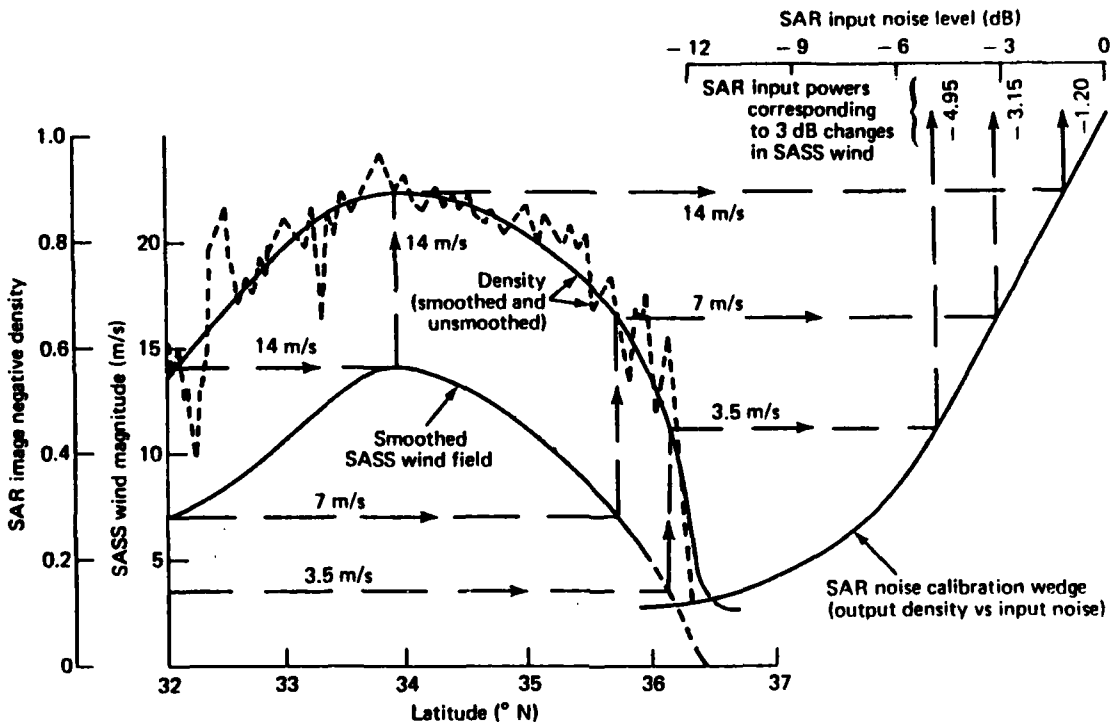
Figure 3a.   Graphical Analysis Relating SAR Backscatter to Sass-Derived
             Winds (After Beal, 1979)
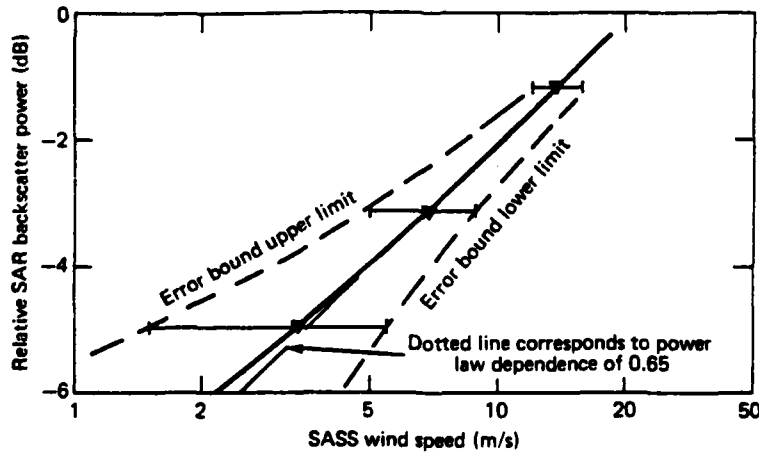
Figure 3b.   Evaluation of Equation 2 Using Data in (a) (After Beal, 1979)
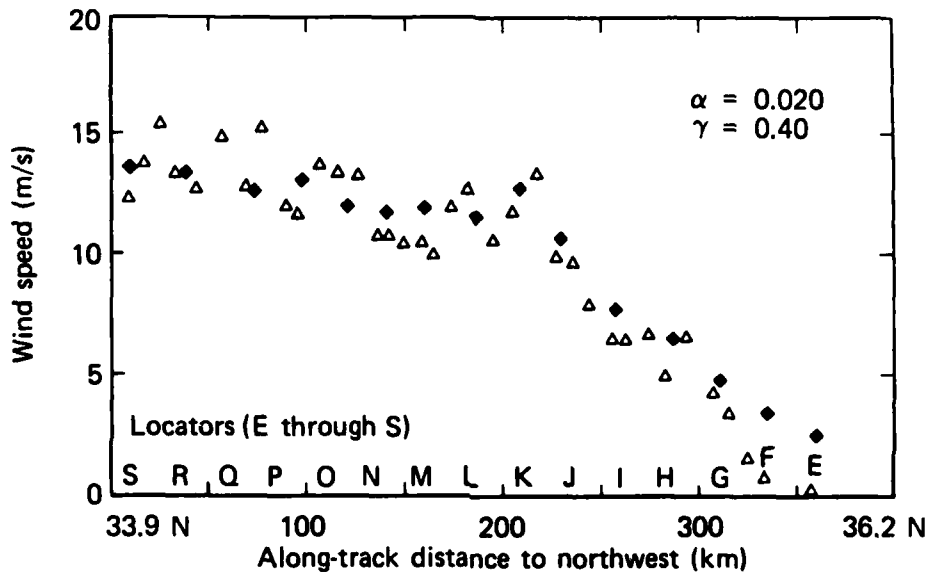
Figure 4.   Comparison of Winds Inferred From SAR
(Δ) and Sass (◆) Data (After Jones,
et. al., 1981)
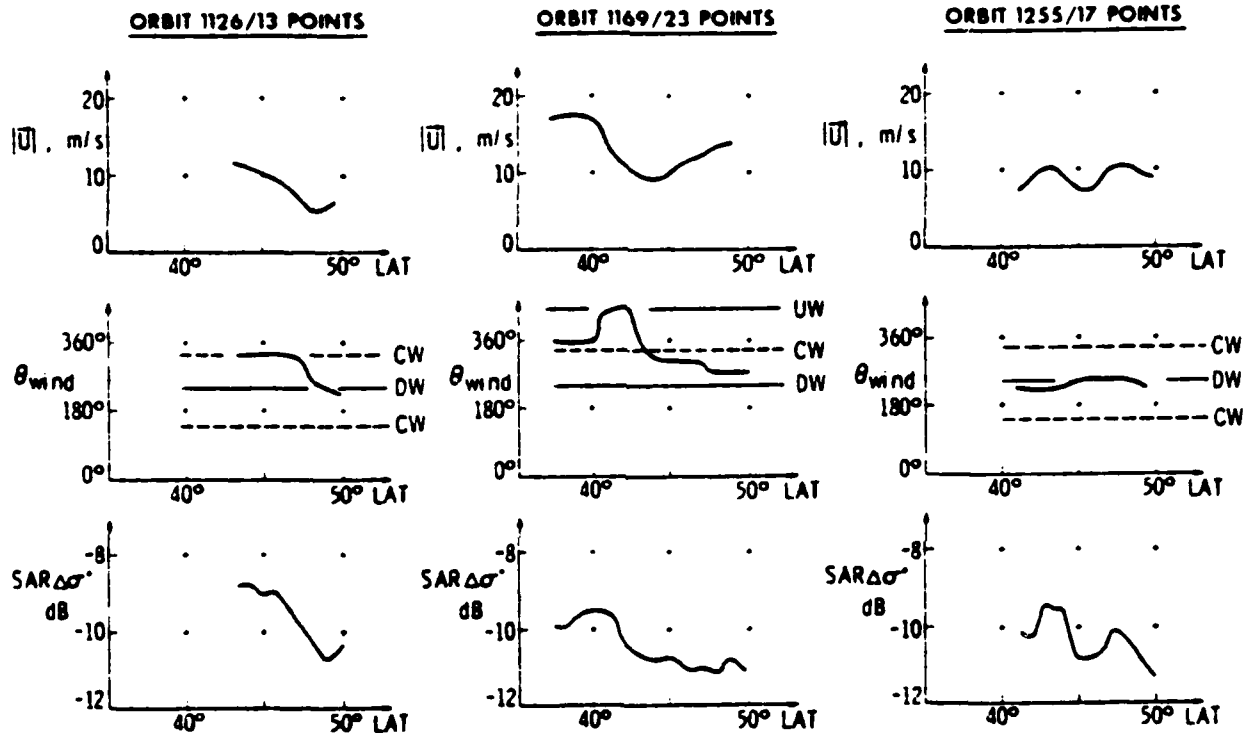
Figure 5. Profiles of Radar Cross Section and Wind Speed for Three
Goasex Revolutions (After Thompson, et al., 1981)

no upwind/downwind anisotropy exists (i.e., $a_2 = 0$). The results of this study indicated a wind speed exponent of 0.5 ± 0.1 and an upwind/crosswind anisotropy coefficient of 0.05 ± 0.05 produced the best results.

Several conclusions can be drawn from the past work in Seasat SAR measurement of ocean surface winds summarized above. At the L-band wavelength of Seasat, the radar backscatter appears to behave nearly isotropically. The method of calculating radar cross section from densitometer measurements of image film appears to introduce some uncertainty into the results of the above studies. This is evidenced by the lack of agreement in the wind speed exponents determined by two different investigators using the same data set. It should be noted that the above Seasat SAR wind studies were performed using only relatively short lengths of data collected during a given revolution, a major goal of this study was to utilize the complete set of data collected during a single revolution (~3900 km).

2.3 SEASAT SAR SYSTEM CONSIDERATIONS

The synthetic aperture radar (SAR) aboard Seasat was an L-band (1.275 GHz, 23.5 cm wavelength), like-polarized (horizontal-transmit, horizontal-receive) system which generated continuous radar imagery with a 100 km ground swath width at a nominal resolution of 25 m from an altitude of 800 km. It collected imagery at an average incidence angle of 22°. The operating parameters for the Seasat SAR are presented in Table 1. For a more detailed discussion on the Seasat SAR and its 99-day mission, the reader is referred to Beal, et al. (1981) or Jordan (1980).

Recall that a synthetic aperture radar such as that on Seasat is a coherent imaging device which uses the Doppler information of a moderately broad physical antenna beam to synthesize a very narrow beam, thus achieving fine azimuthal (along-track) resolution (Harger, 1970; Brown and Porcello, 1969). Fine range (cross-track) resolution

TABLE 1
RADAR PARAMETERS OF SEASAT-A SYNTHETIC APERTURE RADAR (SAR)

Frequency	1274.8 MHz
Wavelength	23.5 cm (L-band)
Polarization	HH
Transmitted Bandwidth	19 MHz
Pulse Duration	33.8 µsec
Pulse Time-Bandwidth Product	642
Transmitter RF Power	800 W Peak – 46 W Average
Transmitter Type	Solid-State Bipolar Transmitter
PRF	1647
Satellite Altitude	~800 km
Nominal Range (20°)	~850 km
Antenna Dimensions	10.7 x 2.16 m
Antenna Beamwidth, Elevation	6°
Antenna Pointing Angle	19-25° off nadir, right side
Surface Resolution	25 m x 25 m (4 look data)
Slant Range Resolution	8 m
Azimuth Resolution (one look)	6.25 m
Integration Time	0.5 to 2.5 sec depending on resolution
Image Swath Width	100 km
Image Length	250 to 4000 km
Sensor Power	60 W, nominal operation
Satellite Velocity	~7000 m/sec

is achieved by transmitting long frequency-dispersed pulses which are later compressed by matched filtering techniques into equivalent short pulses. The data received by the Seasat SAR was transferred to any of several ground stations via a digital data link where it was stored on high density digital tape (HDDT). The HDDT could then be played back and recorded on film (signal film) for optical processing (Kozma, et al., 1972), or transferred to a computer compatible tape (CCT) for digital processing (Wu, et al., 1981). To facilitate optical processing, the signal film is recorded in four quarter swaths. Each quarter swath represents a ground area width of approximately 32 km width, and overlaps the adjacent quarter swath by 6-7 km. The optical processing procedure will be discussed in more detail in the next section.

The wavelength at which the Seasat SAR system operated, 23.5 cm (see Table 1), does not penetrate more than a few centimeters into water. Therefore, the recorded data is primarily reflected from the water surface and is a function of the surface roughness, slope, and motion. The 23.5 cm wavelength also determines the ocean wavelength to which the SAR is most sensitive (Bragg wave). Using Eq. (1), the Bragg wavelength for resonance with the Seasat SAR is approximately 32 cm. This corresponds to the ultra-gravity wave portion of the ocean wave spectrum.

Two considerations must be made when using Seasat SAR data to study ocean surface winds. These are both related to the radiometric fidelity of the Seasat SAR data. Recall that the model which relates surface wind conditions to the SAR data requires that σ_0 be measured. Past SAR/wind studies have inferred σ_0 from densitometer measurements of optically-processed image film. This method assumes linearity in the density vs. log intensity characteristics of the image film. This process can introduce errors into the calculated intensities as discussed by Lyzenga, et al. (1982). The second concerns the along-track radiometric stability of the Seasat SAR data.

15

The azimuth or Doppler spectrum of the signals received by the Seasat SAR is dependent on the antenna gain pattern, the antenna look direction, the platform velocity, and the radial velocity of the objects in the imaged scene. Shifts in this Doppler spectrum in the along-track direction are due to earth rotation effects and spacecraft attitude changes. This shifting, if unaccounted for, can lead to gross errors in the radiometric properties of the image film. The above effects will be discussed in more detail in the following section along with the methods we devised to minimize or eliminate their effect.

3
DATA SET AND MEASUREMENTS

Presented in this section is a description of the Seasat SAR data used in this study, as well as a description of the measurement techniques we employed.

3.1 DATA SET

The Seasat SAR data used in this study were from four Revolutions collected in support of the JASIN experiment (Allan and Guymer, 1980). Three of these data sets (Revs. 547, 633, and 791) were obtained during an ascending pass of about 800 km in extent, lying between the British Isles and Iceland. In contrast, Revolution 757 was a descending pass which contained approximately 3900 km of ocean data extending from Norway to the mid-Atlantic. These revolutions are summarized in Table 2. The ground coverage of the data used in this study are shown along with other Revolutions in Figure 6. These data were recorded onto HDDT's at the Oakhanger, England receiving station, and later played back onto signal film at the Johns Hopkins Applied Physics Laboratory (APL). The extreme length of Revolution 757 created problems in making intensity measurements over the entire pass. These problems and their possible solutions are discussed below.

3.2 INTENSITY MEASUREMENTS

The basic assumption of radar wind studies is that there is a relationship between the normalized radar cross section (σ_0) of the ocean surface and the surface wind speed and direction. The use of SAR image film for measuring winds requires the additional assumption that there is a unique relationship between the image film density and the normalized radar cross section. Although this is true locally, there are systematic effects which cause variations in the

TABLE 2
JASIN SEASAT SAR DATA USED IN WIND STUDY

| Revolution | Collection Date | Length (km) | Range of Wind Conditions[1] | |
			U (m/s)	θ[2] (°True)
547	4 August	820	2.4–7.4	144–185
633	10 August	875	2.7–9.1	306–345
757	18 August	3885	5.0–16.0	330–150
791	21 August	870	5.0–12.0	50–55

1. SASS–derived measurements.
2. Direction wind is blowing.
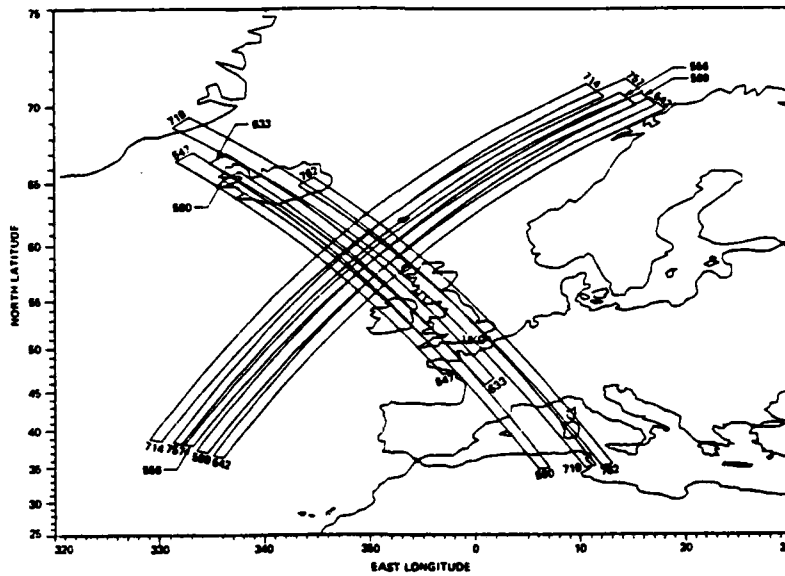
Oakhanger, England: August 4 through August 19
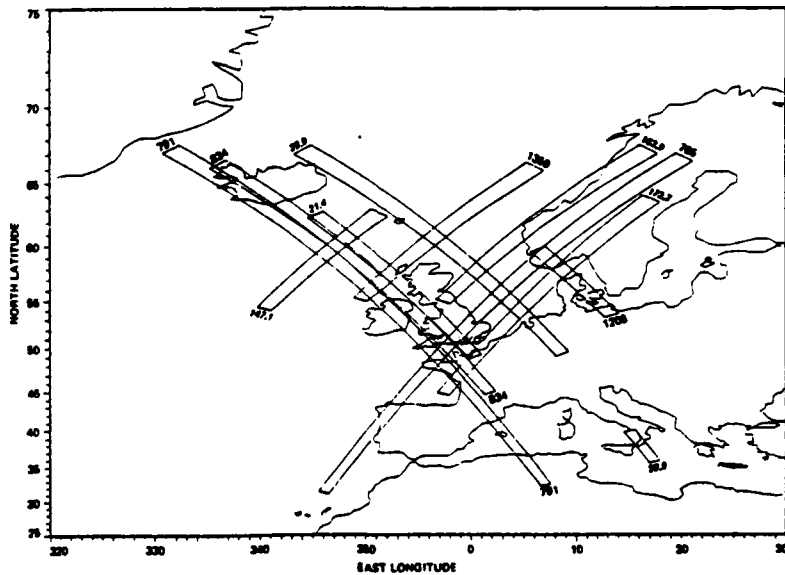
Oakhanger, England: August 20 through October 10

Figure 6. Ground Coverage of Seasat SAR Data Collected at the
Oakhanger, England Receiving Station Including the
Four Revolutions Used in This Study (After
Pravdo, et al., 1983)

19

effective SAR response function both in the across-track and along-
track directions. In order to reduce these effects and also to
eliminate the calibration problems caused by the nonlinear response
of the image film, a special measurement procedure was devised using
the ERIM SAR optical processor.

A diagram of the optical processor is shown in Figure 7. The
raw SAR data is recorded on signal film which is inserted at P_1
and illuminated by a coherent light source. An image of the scene
is reconstructed at P_3 (termed the image plane), and is normally
recorded by placing a film in this plane (Kozma, et al., 1972). To
avoid the nonlinearities involved in this film recording process,
measurements were made directly by placing a photometer probe in this
plane of the optical processor (P_3), and recording the voltage
output on a strip chart. The aperture size of this probe corre-
sponded to a ground area of 2.5 x 2.5 km. The scene was scanned in
the along-track direction by moving the signal film through the pro-
cessor while holding the probe fixed.

A second set of measurements were made in the frequency plane
(P_2) of the processor. The light intensity distribution in the
frequency plane corresponds to the Fourier transform of the signal
histories or of the complex image. Thus, the signal measured by a
probe in this plane corresponds to the energy contained within a
finite frequency interval (defined by the aperture size of the probe)
which is scattered from the entire surface area contained within the
signal plane aperture. This area is approximately 15 km in the
along-track direction by 25 km in the across-track direction. Thus,
the spatial resolution of these measurements is much coarser than
the image plane measurements but corresponds more nearly to the
resolution of the scatterometer. The advantage of these measurements
is that they are less affected by systematic errors due to Doppler
spectrum shifts, as described below.

SAR OPTICAL PROCESSOR
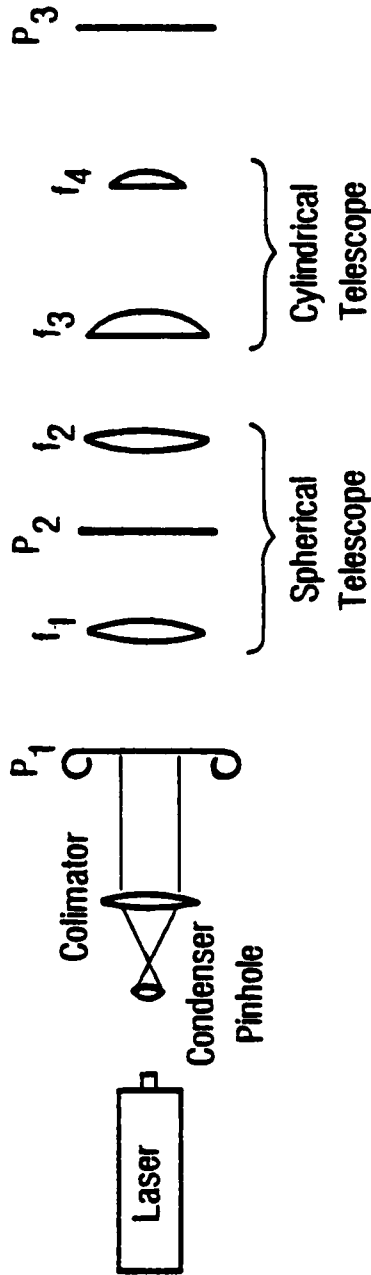
Figure 7. Simplified Schematic Diagram of a SAR Optical Processing System

The Doppler or azimuth frequency spectra for two segments of data from Seasat Revolution 757 are shown in Figure 8. These spectra were obtained by scanning the light intensity distribution in the frequency plane (P_2). These scans show two spectral peaks corresponding to the actual Doppler spectrum and one of the alias spectra which result from the discrete sampling of the signal at the pulse repetition frequency (PRF) of the system. These two spectral peaks would have the same amplitude if they were recorded without distortion. The fact that they are of unequal amplitude is primarily due to the nonuniform frequency response of the recording system.

During normal processing, an aperture is placed in the frequency plane to pass the true spectrum and block out the alias spectra. This is done to avoid azimuth ambiguities in the image. The image intensity is then proportional to the amplitude of the spectrum selected for processing. It is apparent that this amplitude varies as the position of the spectral peak shifts. Thus, the image intensity depends not only on σ_0, but also on the location of the Doppler spectrum, which changes with time due to the earth's rotation and to spacecraft attitude variations. One solution to this problem is suggested by the fact that when the spectrum shifts, a decrease in the amplitude of one of the spectral peaks is accompanied by an increase in the amplitude of the other. Therefore, by integrating over the entire range of frequencies shown in Figure 8, the effect of these variations is minimized. This is accomplished by placing the photometer, with a suitable aperture in the frequency plane (P_2) rather than the image plane (P_3) of the processor, as described above. A second solution is to make explicit corrections to the image plane measurements for the effects of Doppler shifts; this procedure is described in the following section. A more complete discussion on the effects of Doppler spectrum shifting is given in Appendix A.

22
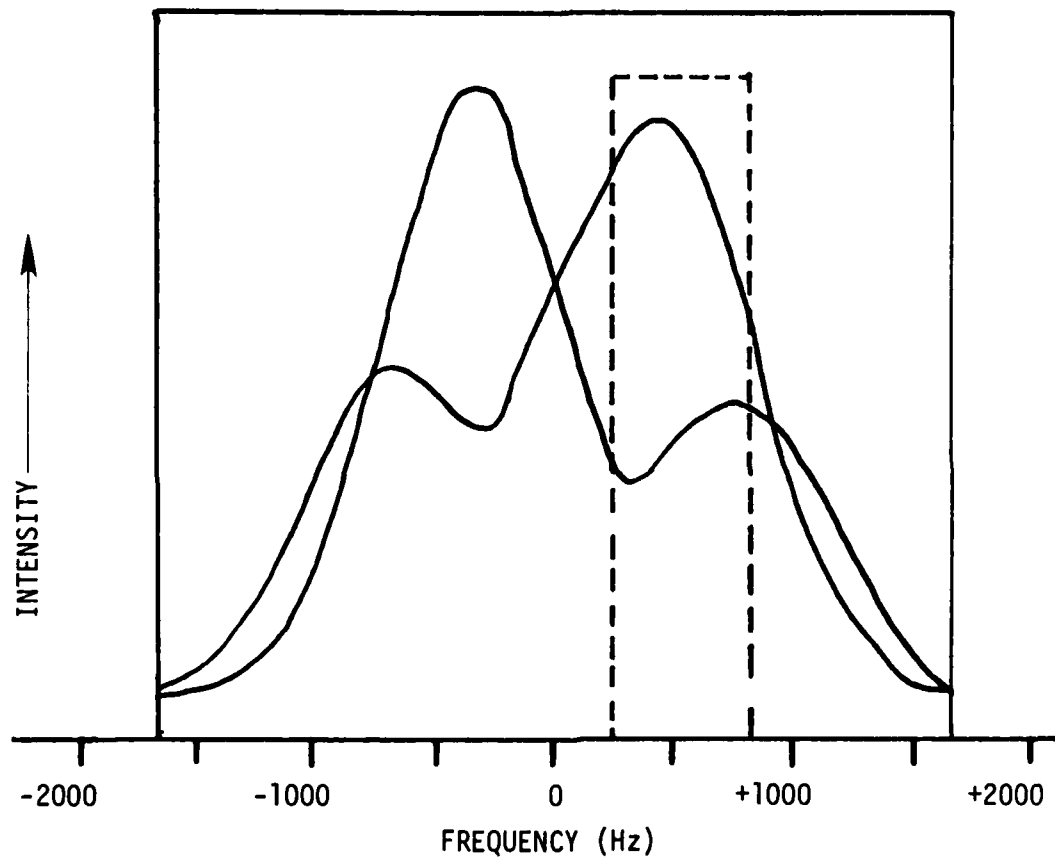
Figure 8.   Doppler Spectrum Scans for Two Sections of
Revolution 757;   Also Shown are the Frequency
Plane Apertures for the Image Plane Measure-
ments (Dashed) and the Frequency Plane
Measurements (Solid)

Measurements were made in both the image and frequency planes of the optical processor for data from Seasat Revolutions 547, 633, 757, and 791. The frequency plane measurements were made with an aperture width of 3300 Hz, i.e., approximately twice the pulse repetition frequency of the Seasat SAR. The image plane measurements were made with a frequency plane aperture extending from 140 to 810 Hz. The effective frequency plane aperture size for both measurement techniques is indicated on Figure 8. These measurements include an appreciable amount of noise, mainly due to stray light in the processor. The noise level was measured by recording the light intensity with no signal input, and was subtracted from the rest of the data. Plots of the signal intensity at both the frequency and image planes after subtraction of the noise are shown in Figures 9-12. These data are plotted versus time (min X100), which is equivalent to the along-track coordinate for each quarter swath. The effect of Doppler spectrum shifting is particularly noticeable when comparing the image and frequency plane measurements from Revolution 757. The image plane measurements decrease with distance along-track and must be corrected prior to quantitative comparisons with surface wind conditions. The results of comparing these measurements to SASS-derived surface winds using Eq. (2) are presented in the next section.
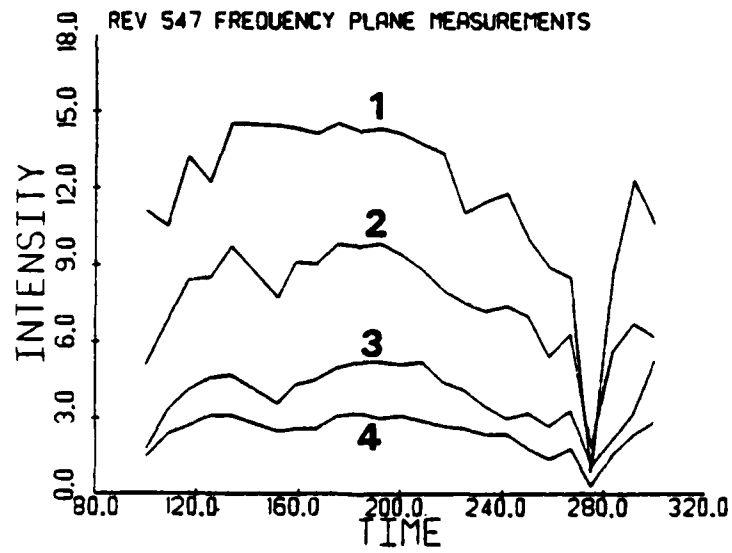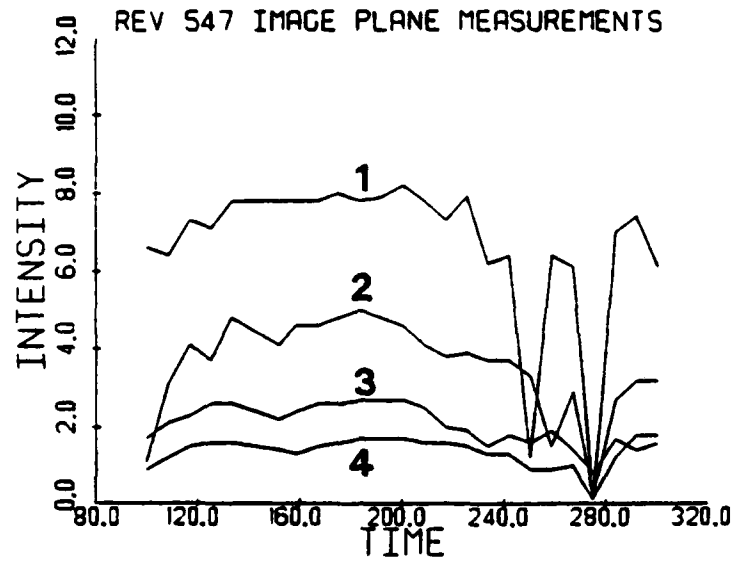
Figure 9. Intensity Measurements Made at the Image and Frequency
           Planes of the SAR Optical Processor for Revolution 547
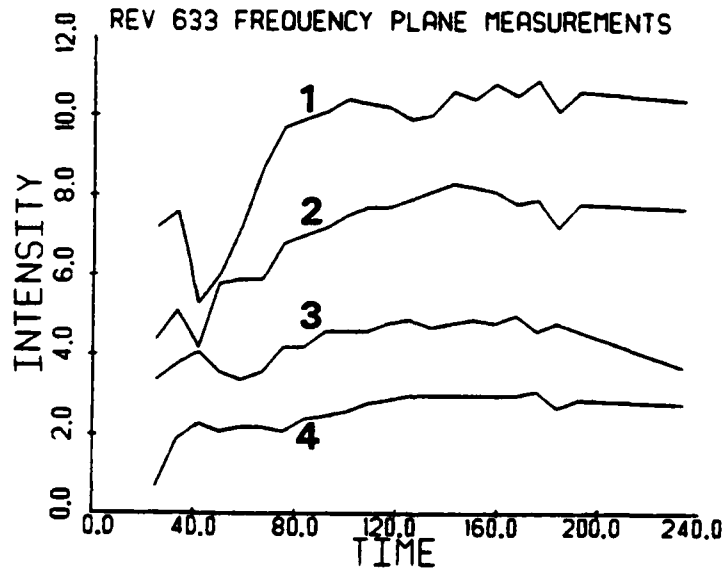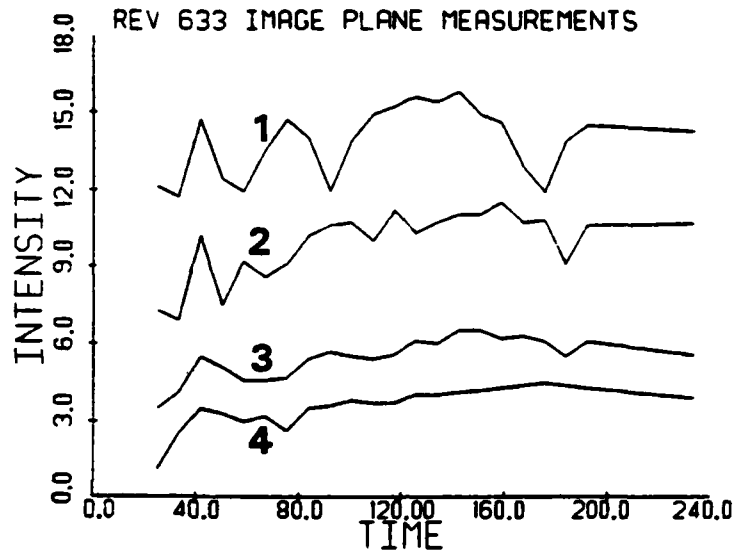
Figure 10. Intensity Measurements Made at the Image and Frequency Planes of the SAR Optical Processor for Revolution 633
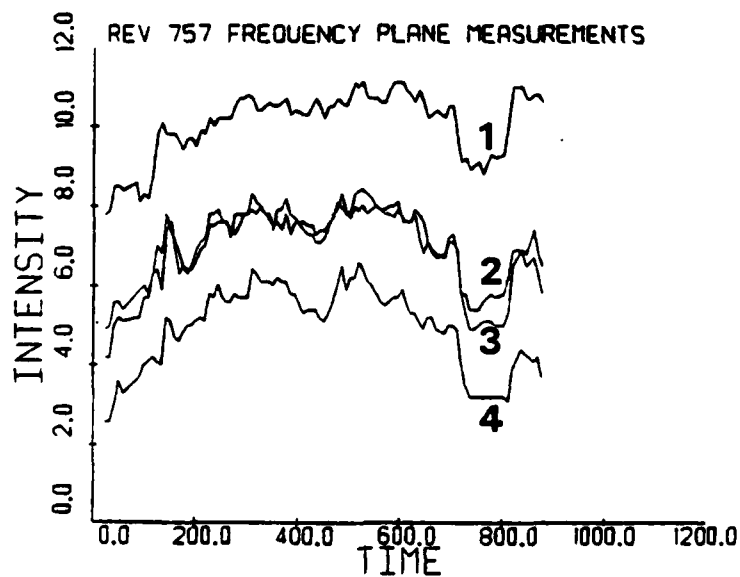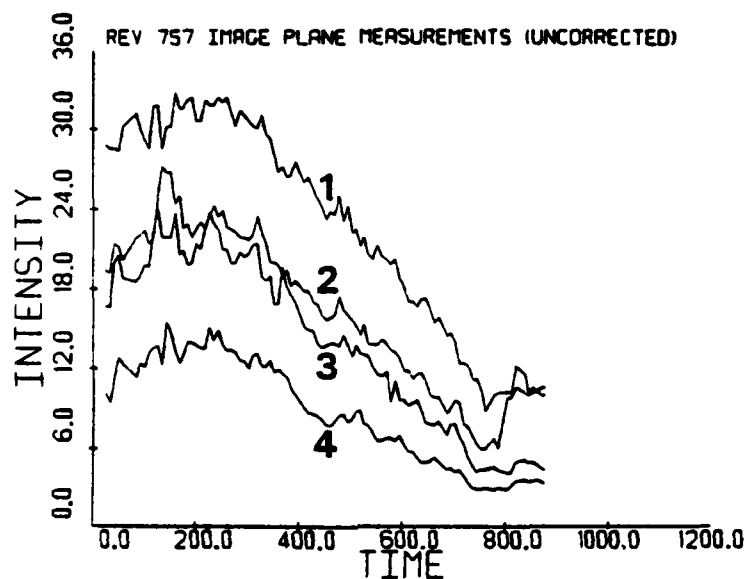
Figure 11. Intensity Measurements Made at the Image and Frequency
Planes of the SAR Optical Processor for Revolution 757

REV 791 IMAGE PLANE MEASUREMENTS
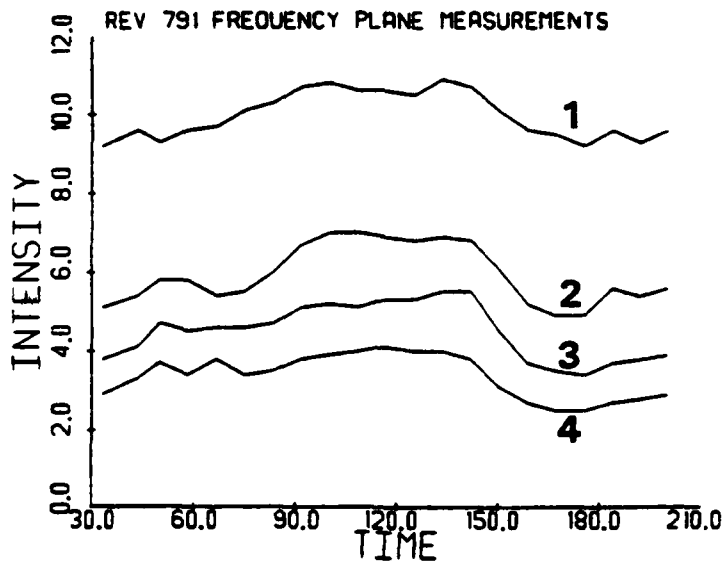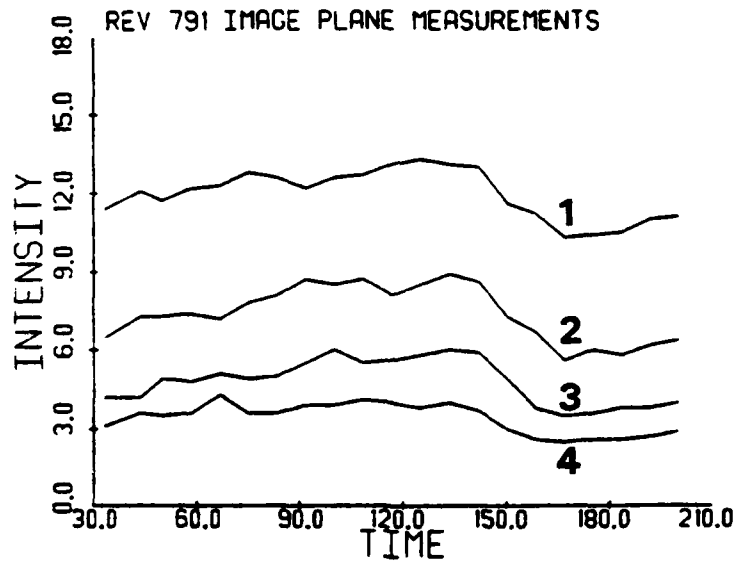
Figure 12. Intensity Measurements Made at the Image and Frequency
Planes of the SAR Optical Processor for Revolution 791

4
ANALYSIS AND RESULTS

The SAR intensity measurements described in the previous section were used to evaluate the SAR/wind model given as Eq. (2). The model coefficients we calculated were then used to predict wind speeds for a section of the data. Additionally, a theoretical scattering model was compared with our results.

4.1 SAR/WIND MODEL RESULTS

The SAR intensity measurements described in the previous section were used to evaluate the SAR/wind model given as Eq. (2). Simple transformation of Eq. (2) leads to

$$\log_{10} \left[\frac{\sigma_0}{(1 + \alpha_1 \cos \psi + \alpha_2 \cos 2\psi)} \right] = \gamma \log_{10} U + C , \quad (3)$$

where C is a constant, σ_0 is the normalized radar cross section, U is the wind speed, γ is the wind speed exponent, α_1 and α_2 are anisotropy coefficients, and ψ is the radar line-of-sight relative to upwind. This equation was evaluated using linear regression techniques for values of α_1 ranging from 0.0 to 0.2 at increments of 0.02, and values of α_2 ranging from 0.0 to 0.8 at increments of 0.05. The wind speed exponent term was determined from the slope of the regression of the combination of terms which produced the highest correlation coefficient (R), which is defined as the covariance of the left and right hand sides of Eq. (3), divided by the product of their individual variances. This coefficient gives a measure of the linear relationship between the two sides of the equation.

The wind data that were used in the above statistical calculations were obtained from measurements made by the Seasat scatterometer system (SASS) coincident with the SAR data. The SASS is a microwave radar which was designed to provide global, day or

night measurements of synoptic scale ocean surface wind. The SASS operated at K_u-band (2.1 cm wavelength) and achieved a spatial resolution of about 50 km. For a more complete description of the SASS, the reader is referred to Jones, et al. (1979).

The SASS data for the four revolutions used in our study were processed at NASA Langley Research Center. The geophysical algorithm which is used to infer wind speed and direction from the SASS measurements recovers between one and four wind vector solutions for each resolution cell. These solutions are nearly equal in velocity, but can vary widely in direction. This result, referred to as aliasing, necessitates additional information (e.g., surface measurements) to yield the correct result. The SASS data used here were de-aliased using local weather maps and should have an inherent accuracy of ± 2 m/s for wind speed and $\pm 20°$ for direction (Jones, et al., 1979). The evaluation of one microwave instrument using the results of another is not a recommended practice, but was necessary in this study due to the lack of sufficient surface measurements.

The SAR/wind model presented in Eq. (3) requires as input the normalized radar cross section (σ_0); we have used what is more accurately termed a relative radar cross section measure. This is due to the non-calibrated nature of Seasat SAR data. Care has been taken to make these measurements at a constant range location. Thus, radiometric effects such as the antenna gain pattern, R^3 power loss, and the sensitivity time control which all vary in range can be ignored. The use of this relative measure, however, should not alter the results of this study since we are not concerned with the so-called intercept value C from our regression analysis of Eq. (3), but only with the γ term for a given α_1 and α_2. That is, assuming we have both a SAR intensity profile and appropriate γ term, we would still need a single surface wind speed in order to determine a wind speed profile.

It should be noted that the above discussion on determining a
wind speed profile from SAR intensity values assumes that the data
is isotropic (i.e., $\alpha_1 = \alpha_2 = 0$). Clearly, if the scattering is
anisotropic, than we are left with one equation containing two un-
knowns. In this case, variations in the SAR measured backscatter
could be caused by a change in either wind speed or direction, or
both. The degree to which the data behaves anisotropically will
ultimately decide the utility of SAR intensity measurements to infer
wind speed. Presented below is an evauation of Eq. (3) for the four
data sets being studied assuming both isotropic and directionally-
dependent behavior.

4.1.1 REVOLUTION 547

The SASS-derived wind conditions for 4 August 1978 during Revo-
lution 547 are shown graphically in Figure 13. Each arrow lies in
the center of the appropriate SAR swath and portrays both wind speed
and direction. These wind conditions are shown plotted in Figure
14. These plots were produced by averaging the wind conditions of
all four swaths for the entire length of the data studied. It should
be noted that all four swaths agreed closely and that the correla-
tions of the SAR and SASS data were performed using the original un-
averaged wind data. The wind speed is seen to range from about 2.4
to 7.4 m/s, while the direction varies from about 144 to 185°. The
SAR measurements corresponding to these data are shown plotted in
Figure 15 for both image and frequency planes, all 4 quarter swaths.
Evaluation of Eq. (3) for both the isotropic and non-isotropic cases
leads to the results presented in Table 3. These results show that
the correlation between radar backscatter and wind speed is very low.
It should also be noted that this correlation does not improve when
directional effects are considered.
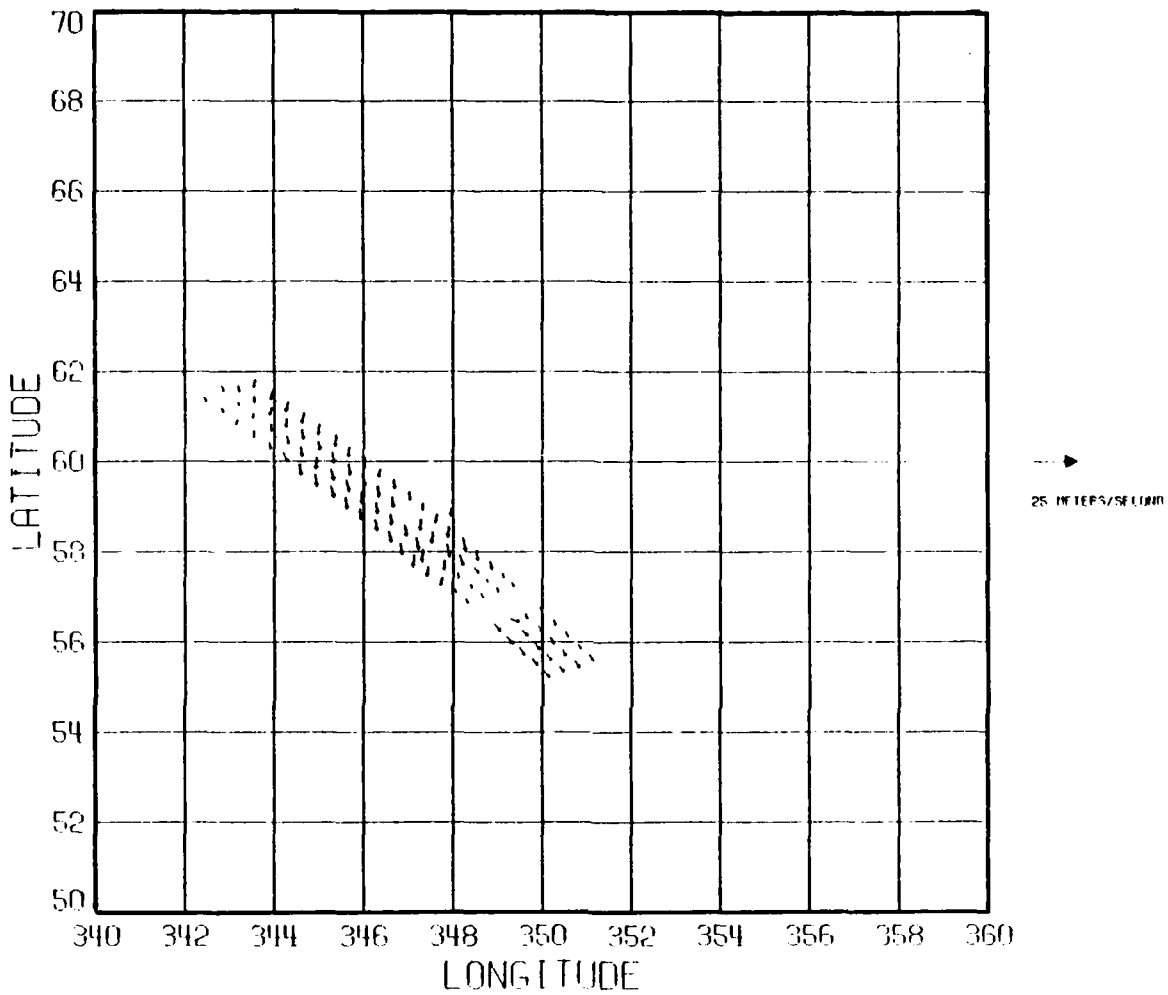
Figure 13.   Graphical Depiction of Sass-Derived Winds for
              Revolution 547

32

REV 547 WIND SPEED

REV 547 WIND DIRECTION
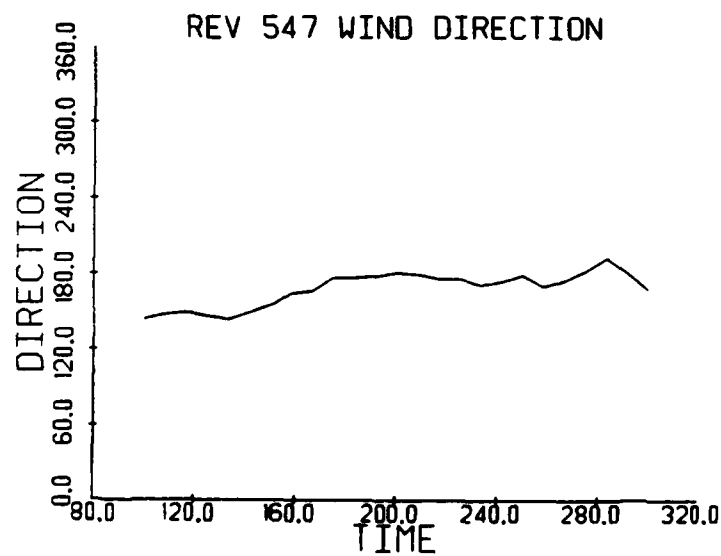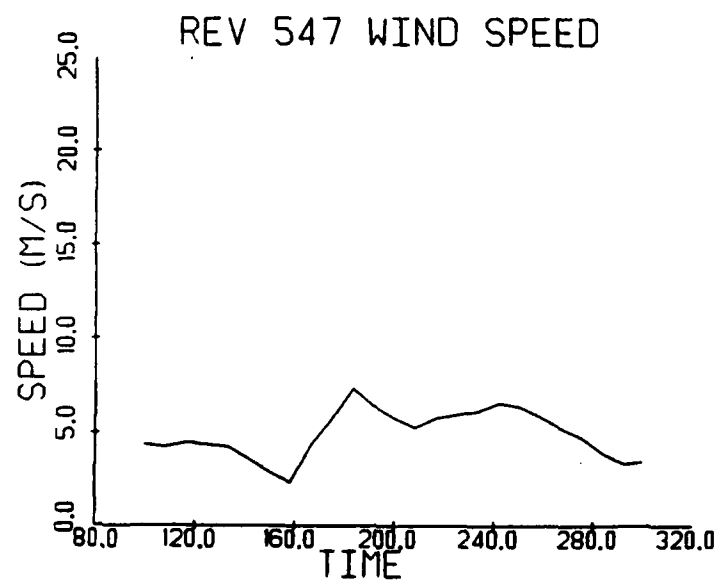
Figure 14.   Sass-Derived Wind Conditions for Revolution 547

REV 547 IMAGE PLANE MEASUREMENTS

REV 547 FREQUENCY PLANE MEASUREMENTS
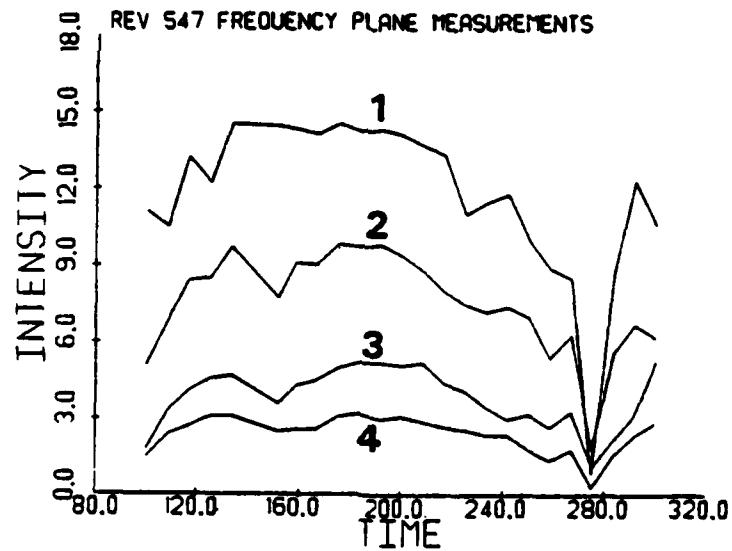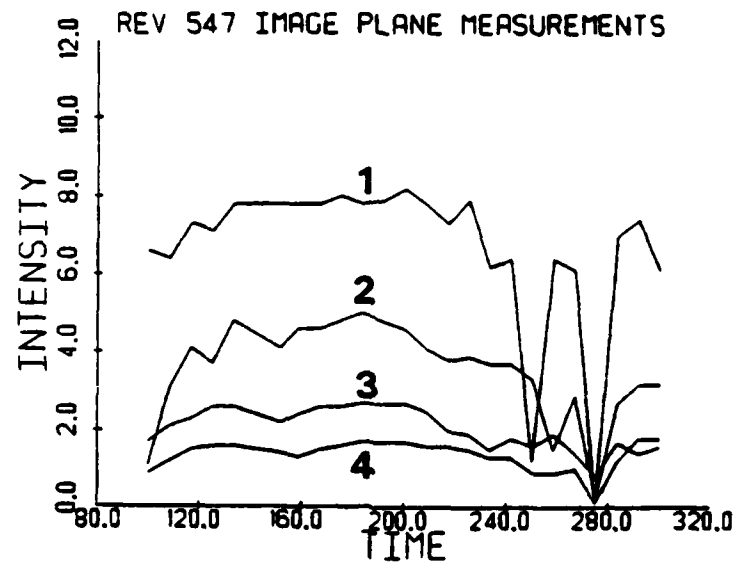
Figure 15.   Intensity Measurements Made at the Image and
             Frequency Planes of the SAR Optical Processor
             for Revolution 547

34

TABLE 3
OPTIMIZED MODEL PARAMETERS AND CORRELATION COEFFICIENTS
FOR REVOLUTION 547

Isotropic ($\alpha_1 = \alpha_2 = 0$)

	Image Plane Sub-Swath				Frequency Plane Sub-Swath			
	1	2	3	4	1	2	3	4
R	0.02	0.14	0.0	0.23	0.14	0.23	0.01	0.29
γ	0.05	0.28	0.0	-0.44	0.22	0.24	0.01	-0.47

Non-Isotropic

	Image Plane Sub-Swath				Frequency Plane Sub-Swath			
	1	2	3	4	1	2	3	4
R	0.02	0.14	0.0	0.23	0.14	0.23	0.01	0.29
γ	0.05	0.28	0.0	-0.44	0.22	0.24	0.01	-0.47
α_1	0.0	0.0	0.0	0.0	0.0	0.0	0.0	0.0
α_2	0.0	0.0	0.0	0.0	0.0	0.0	0.0	0.0

The low correlations for this data set are probably caused by the low wind speed conditions and the presence of non-wind related surface features. During Revolution 547, the surface wind speed averaged only about 5 m/s; perhaps this is below a threshold of detectability for the 23.5 cm wavelength SAR. The SASS aboard Seasat operated at 2.1 cm wavelength, and was only able to detect winds of 2.5 m/s and higher. The plots presented in Figure 15 show a sharp drop in intensity in quarter swaths 1 and 2 for both image and frequency plane measurements. In fact, the image plane measurements of swath 1 show two sharp dips in intensity. The corresponding imagery from this revolution is shown in Figure 16. The two areas of low return are clearly visible. The exact cause of this is unknown, but note their presence apparently had little effect on the SASS data either because of the difference in wavelength or the difference in resolution between the SASS and the SAR.

To further investigate the cause of these low return areas, data collected simultaneously by the Seasat scanning multichannel microwave radiometer (SMMR) was studied. The SMMR is a 5-frequency imaging microwave radiometer which measures dual-polarized microwave radiation from the earth's atmosphere and surface at frequencies of 6.6, 10.7, 18.0, 21.0, and 37.0 GHz (Gloersen and Barath, 1977). The SMMR data can be used to derive several geophysical parameters including: sea surface speed, sea surface temperature (SST), and rain fall rate. The resolution of the SMMR ranges from about 27 km for the 37 GHz channel to about 150 km for the 6.6 GHz channel. It was hoped that the SMMR data from Revolution 547 could help explain the two dark anomalous areas on the SAR imagery discussed above. Presented in Figures 17-19 are the SMMR-derived values for wind speed, sea surface temperature, and rainfall rate for Revolution 547 (Anonymous, 1980). Also shown on each plot is the center of each SAR quarter swath where intensity measurements were made. Examination of these reveals very little that could help to explain the anomalous SAR patterns. This could be due in part to the low resolution of the SMMR data.

RADAR LOOK DIRECTION ⟶
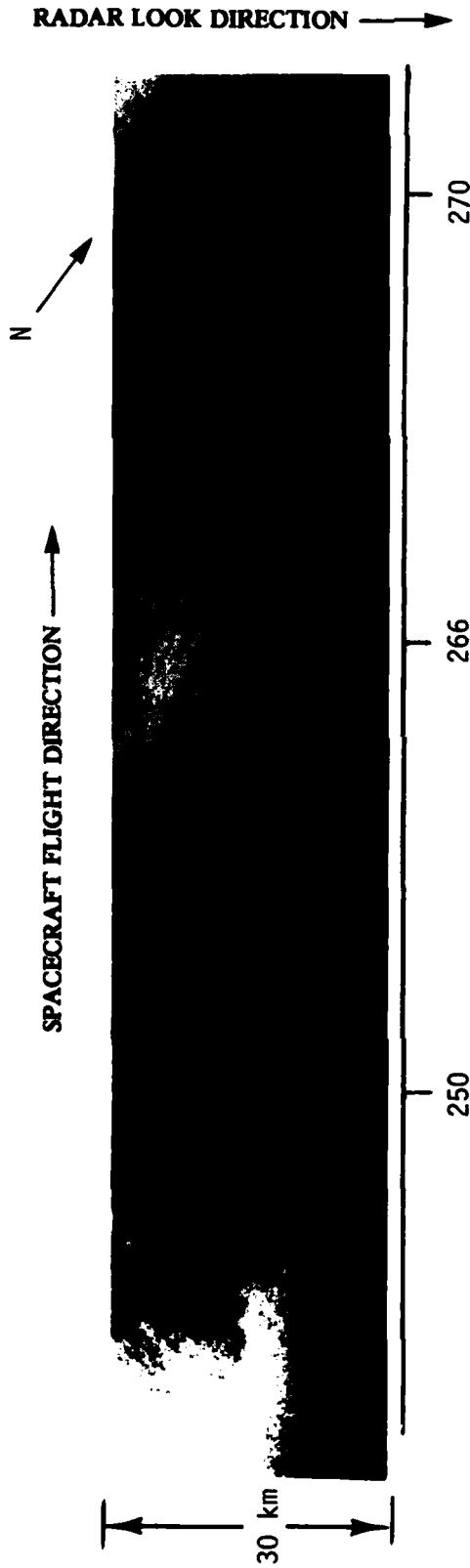
Figure 16. Seasat SAR Image From a Portion of Quarter Swath 1, Revolution 547
Showing Two Regions of Low Return
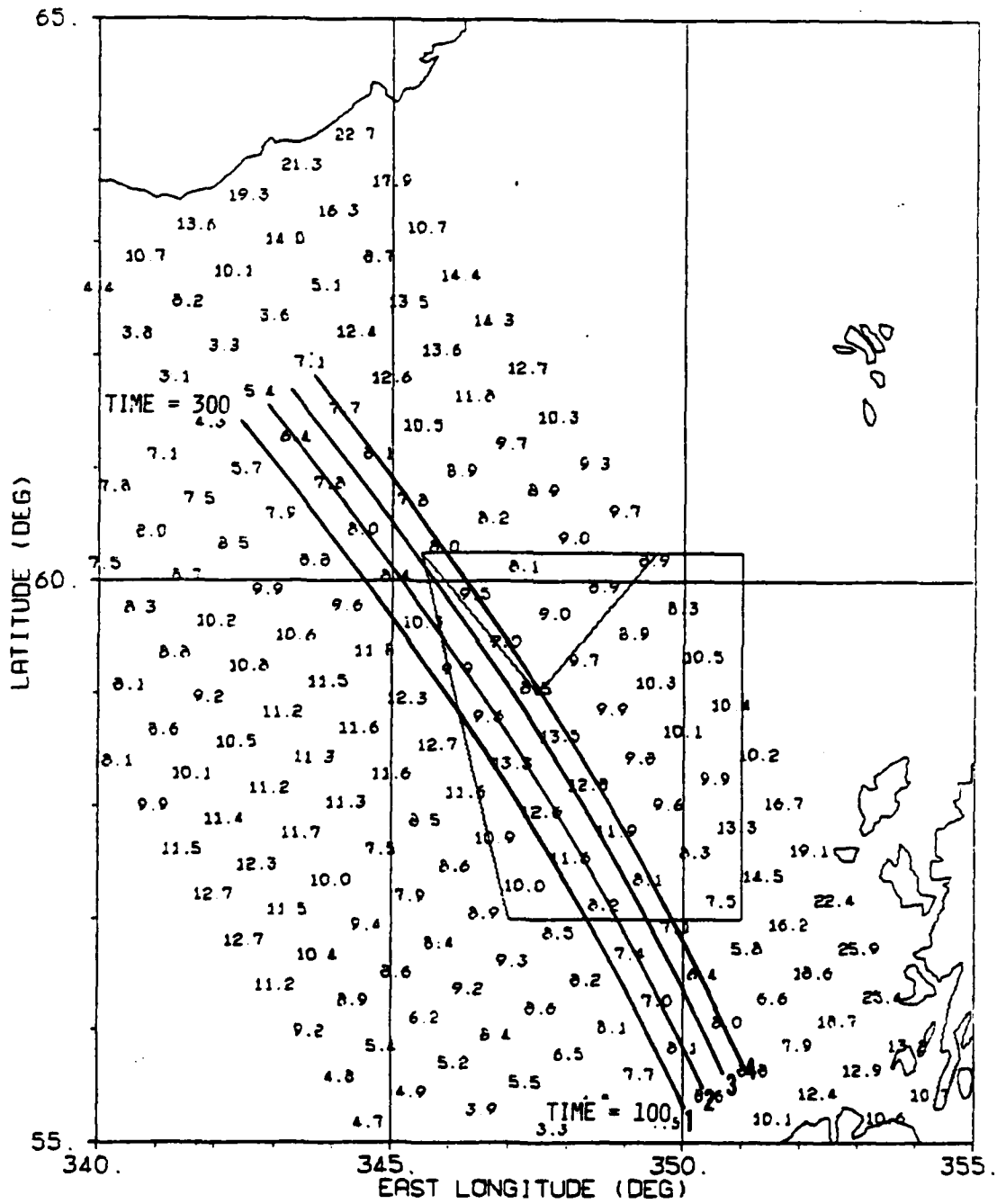
Figure 17.   SMMR-Derived Wind Speeds (M/S) for Revolution 547
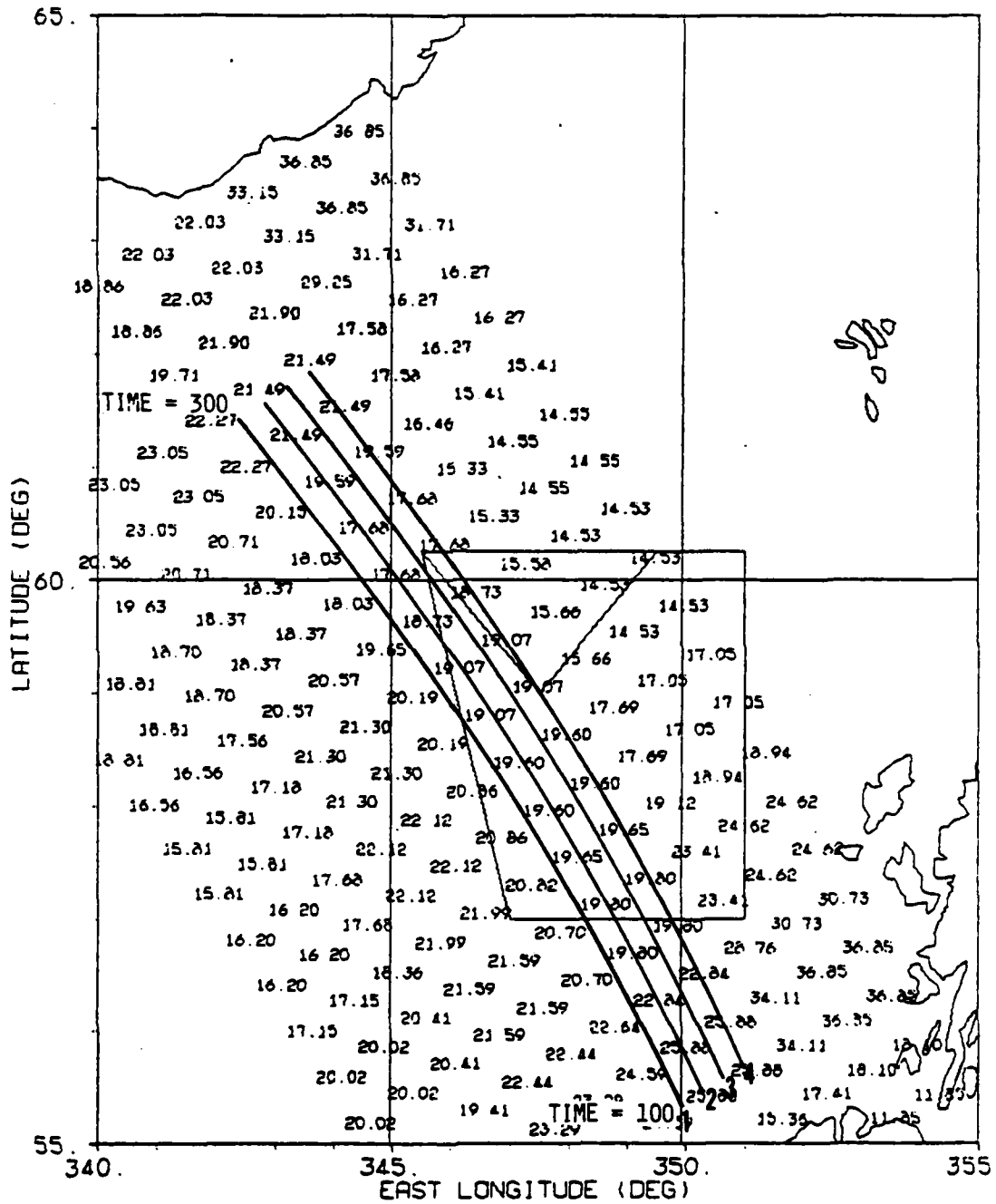
Figure 18. SMMR-Derived Sea Surface Temperatures (°C) for
           Revolution 547
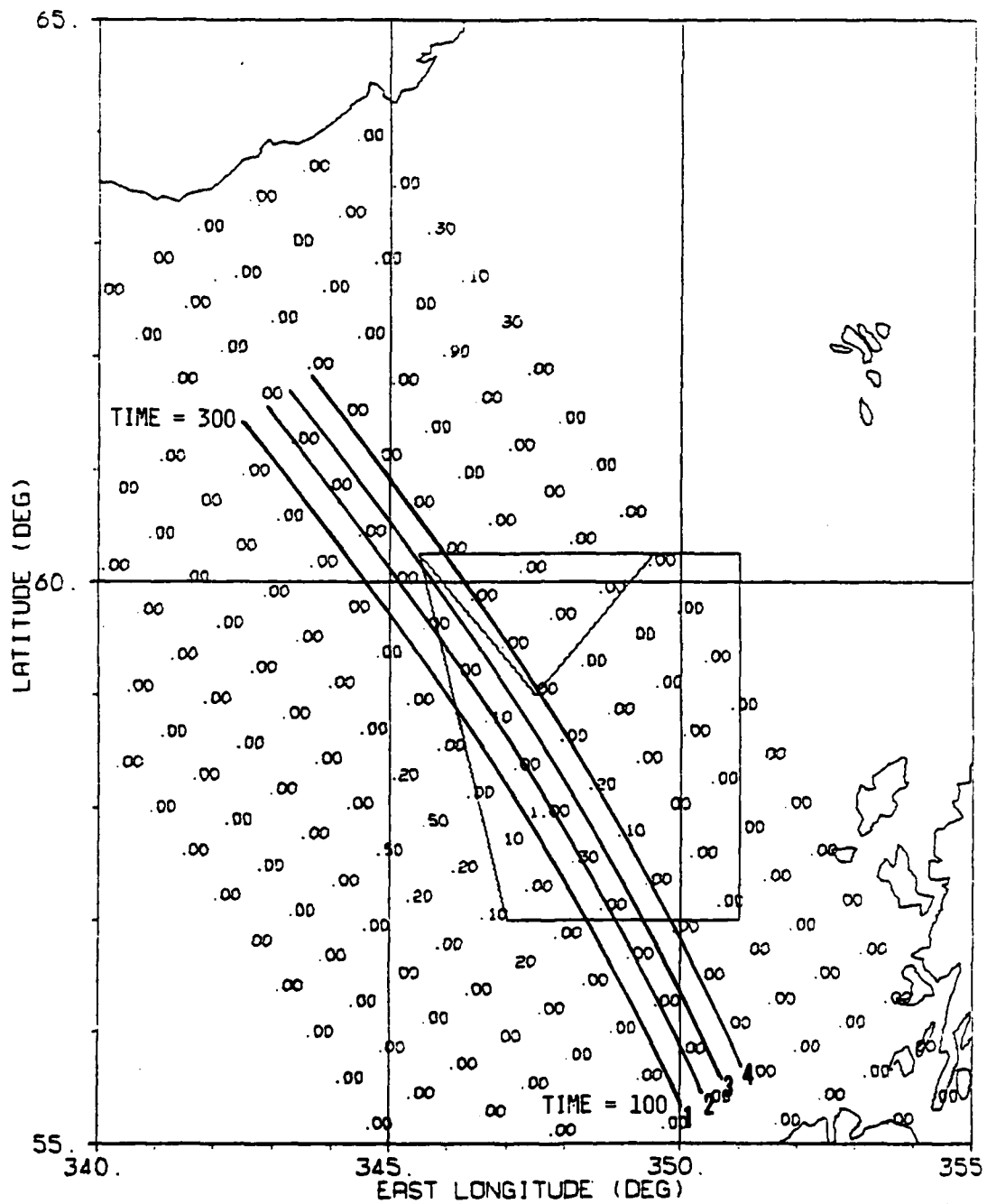
Figure 19. SMMR-Derived Rain Rates (mm/hr) for Revolution 547

4.1.2 REVOLUTION 633

Wind data derived from SASS measurements, collected 10 August 1978 during Revolution 633 are shown graphically in Figure 20 and are plotted in Figure 21. The wind speed ranges from about 2.7 to 9.1 m/s and varies approximately 40° in direction over the length of the pass. The SAR measurements corresponding to these data are plotted in Figure 22 for both image and frequency planes, all four quarter swaths. Evaluation of Eq. (3) using these data leads to the results presented in Table 4. In general, the correlations were quite good, with correlation coefficients larger than 0.8 except for quarter swath 1, which appeared to yield anomalous results for the image plane measurements. Additionally, very little improvement is gained by including directional information in the analysis. Except for the image plane quarter swath 1 results, all wind speed exponents fall within or close to the 0.3 to 1.0 range reported by past investigators (Jones, et al., 1981; Thompson, et al., 1981; Beal, 1979).

4.1.3 REVOLUTION 757

The SASS-derived wind data from 18 August 1978 collected during Revolution 757 are shown graphically in Figure 23 and are plotted in Figure 24. These data extend over 3800 km and are seen to range from 5 to 16 m/s in speed and vary over 180° in direction. The SAR measurements corresponding to these data are shown plotted in Figure 25 for both image and frequency planes, all four quarter swaths. As discussed in the previous section, the image plane measurements for this length of data are severely affected by a shifting of the Doppler spectrum as the latitude of the spacecraft changes. Results of evaluating Eq. (3) using this uncorrected data are presented in Table 5 for both the image and frequency plane cases. Except for quarter swath 1, the frequency plane data correlates more closely with the wind data. Also, the wind speed exponents for the image plane data

41
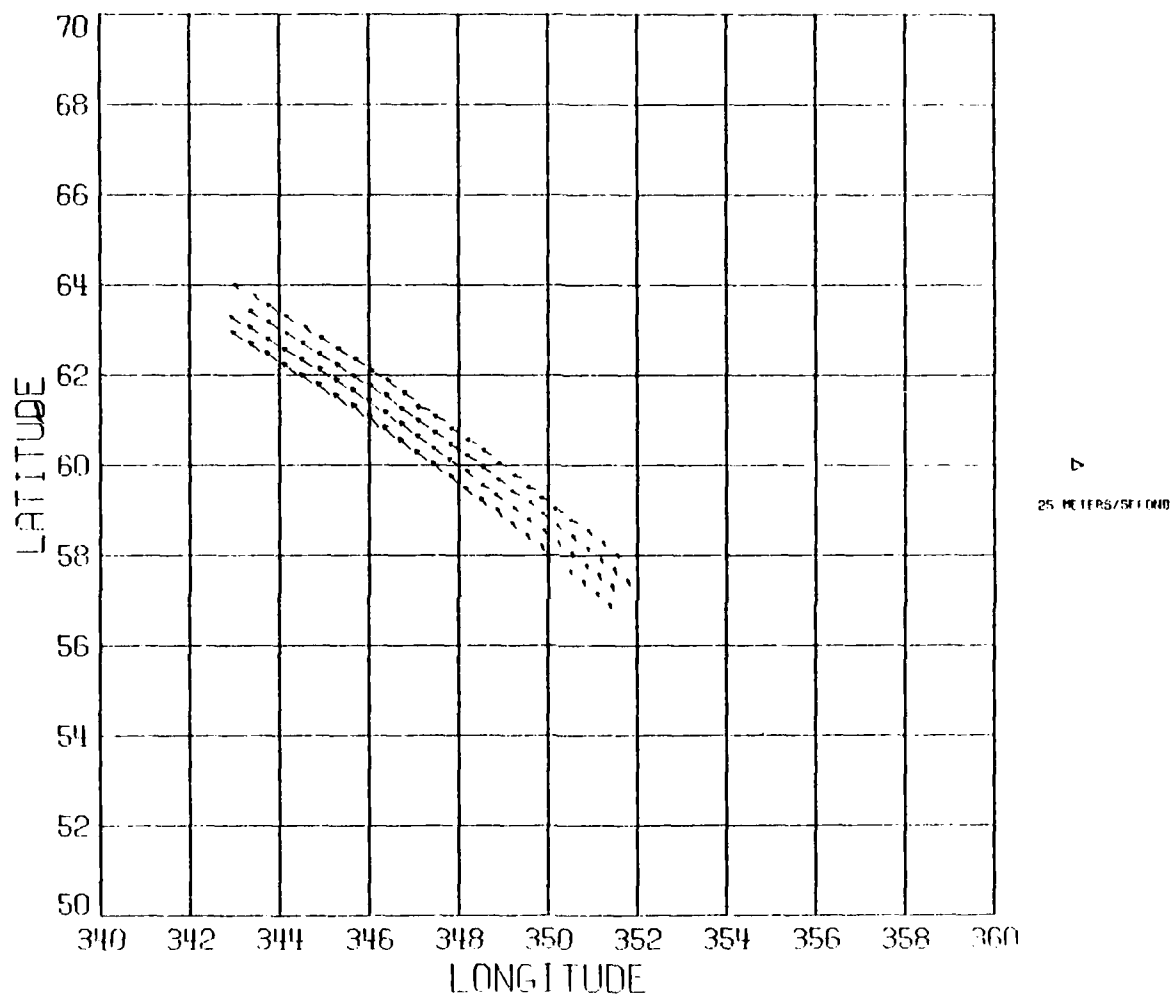
Figure 20. Graphical Depiction of SASS-Derived Winds for
Revolution 633

REV 633 WIND SPEED

REV 633 WIND DIRECTION
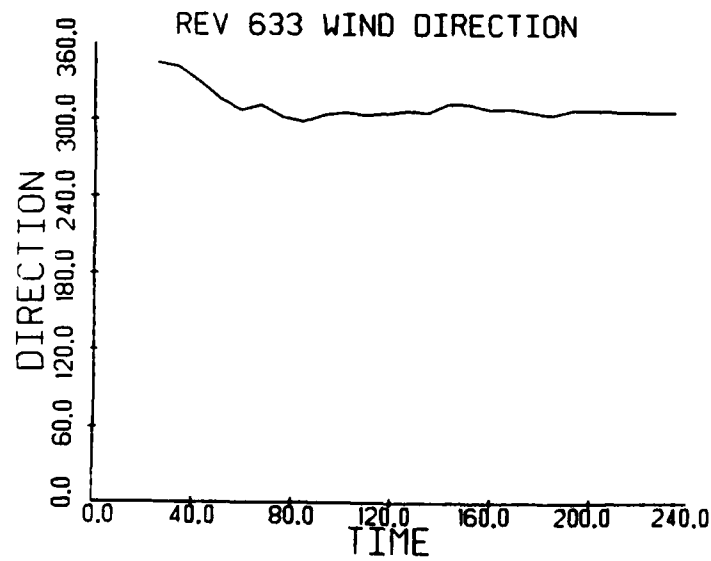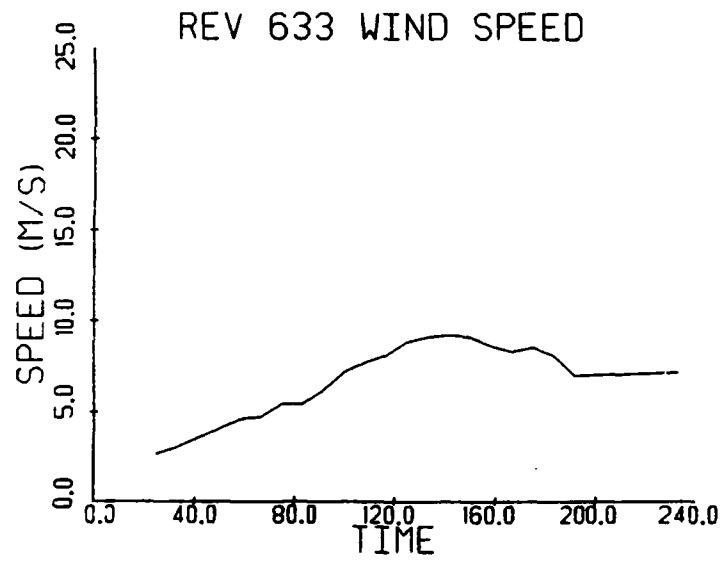
Figure 21.   SASS-Derived Wind Conditions for
Revolution 633

43
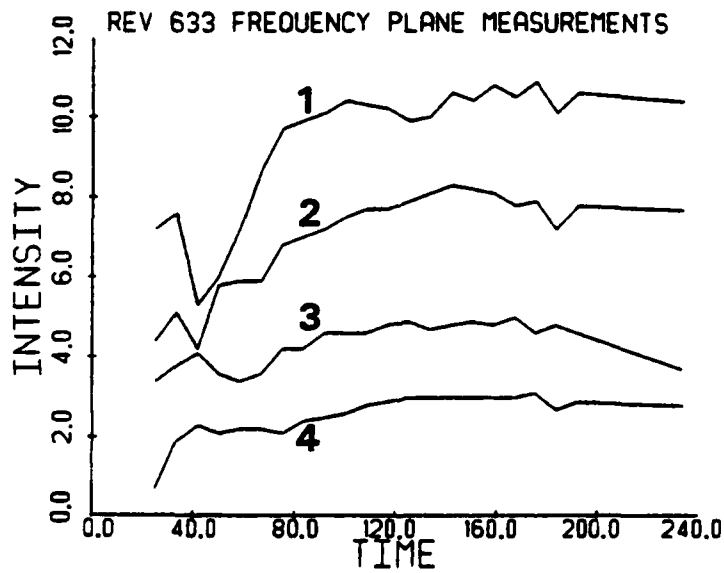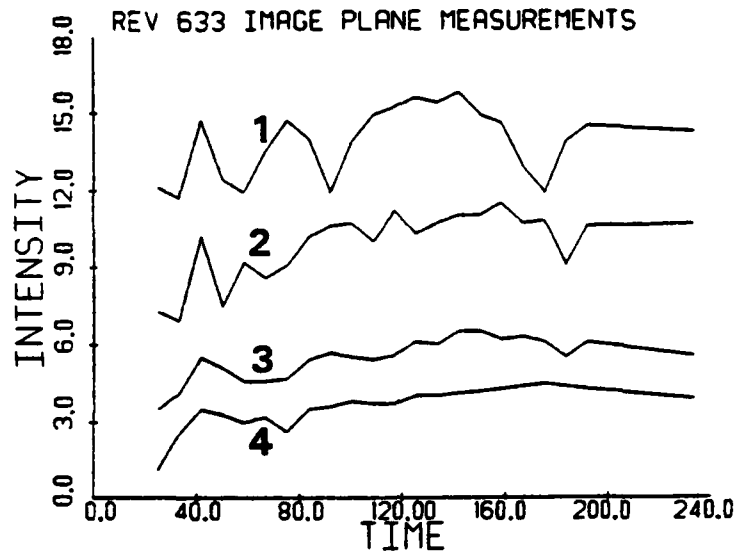
Figure 22. Intensity Measurements Made at the Image and Frequency Planes of the SAR Optical Processor for Revolution 633

44

TABLE 4
OPTIMIZED MODEL PARAMETERS AND CORRELATION COEFFICIENTS
FOR REVOLUTION 633

Isotropic ($\alpha_1 = \alpha_2 = 0$)

	Image Plane Sub-Swath				Frequency Plane Sub-Swath			
	1	2	3	4	1	2	3	4
R	0.59	0.81	0.87	0.86	0.85	0.94	0.84	0.86
λ	0.14	0.25	0.35	0.91	0.42	0.41	0.28	0.95

Non-Isotropic

	Image Plane Sub-Swath				Frequency Plane Sub-Swath			
	1	2	3	4	1	2	3	4
R	0.72	0.81	0.87	0.86	0.91	0.95	0.85	0.86
γ	0.14	0.25	0.35	0.91	0.58	0.40	0.29	0.95
α_1	0.0	0.0	0.0	0.0	0.0	0.04	0.0	0.0
α_2	0.6	0.0	0.0	0.0	0.6	0.4	0.5	0.0
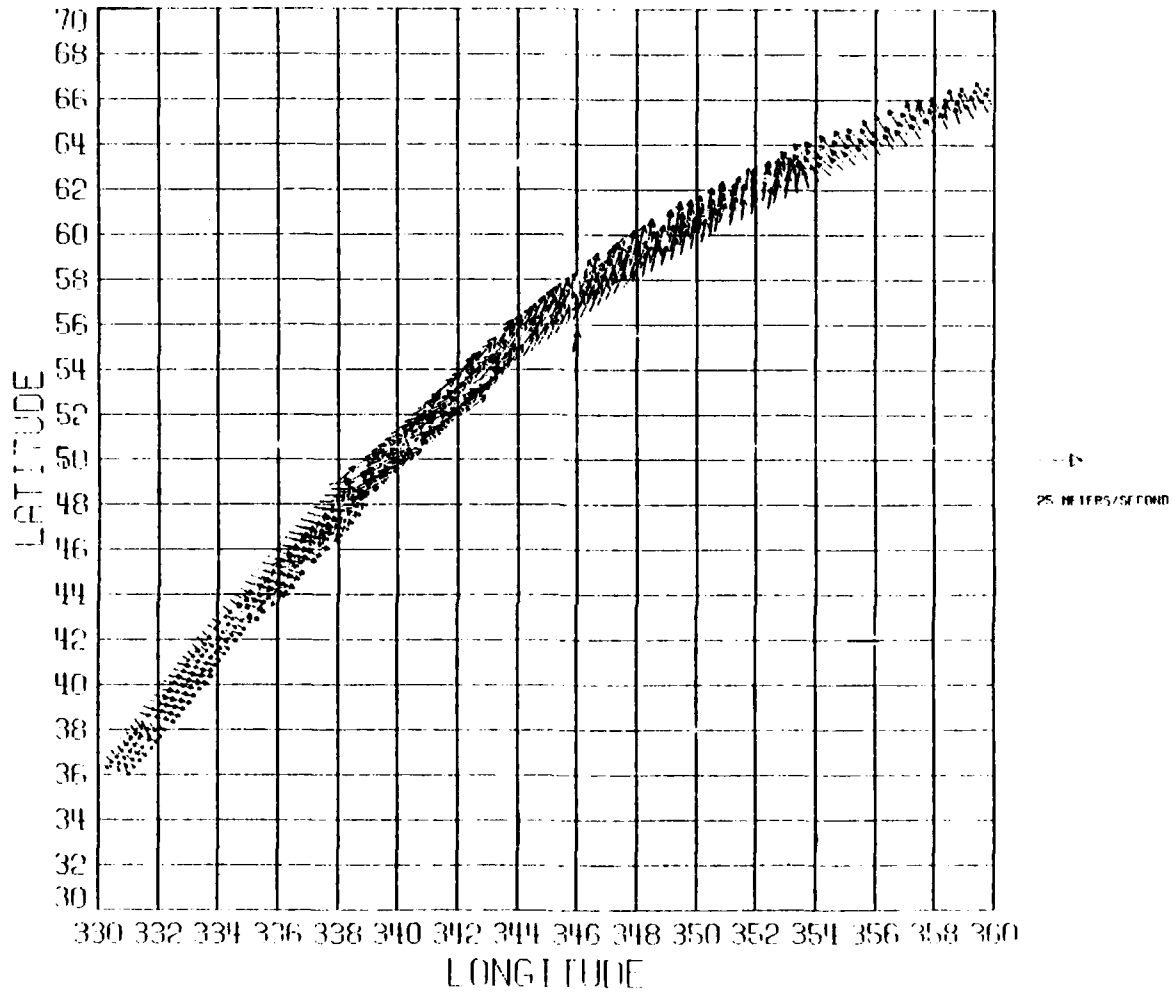
Figure 23.   Graphical Depiction of SASS-Derived Winds
for Revolution 757

REV 757 WIND SPEED

REV 757 WIND DIRECTION
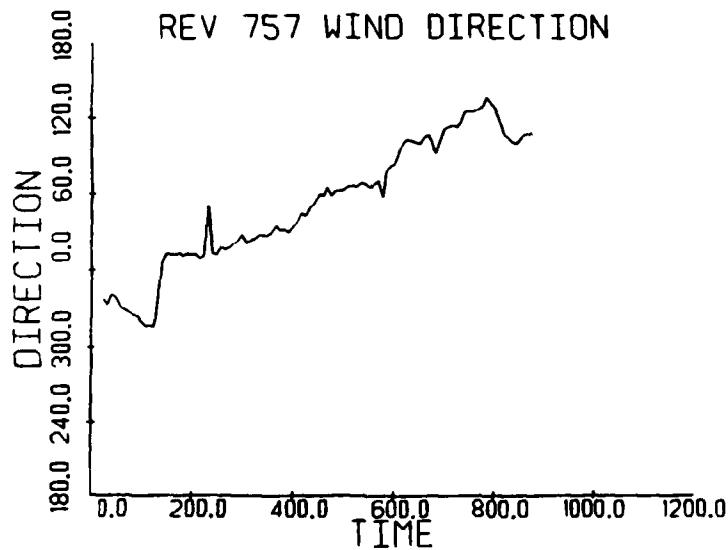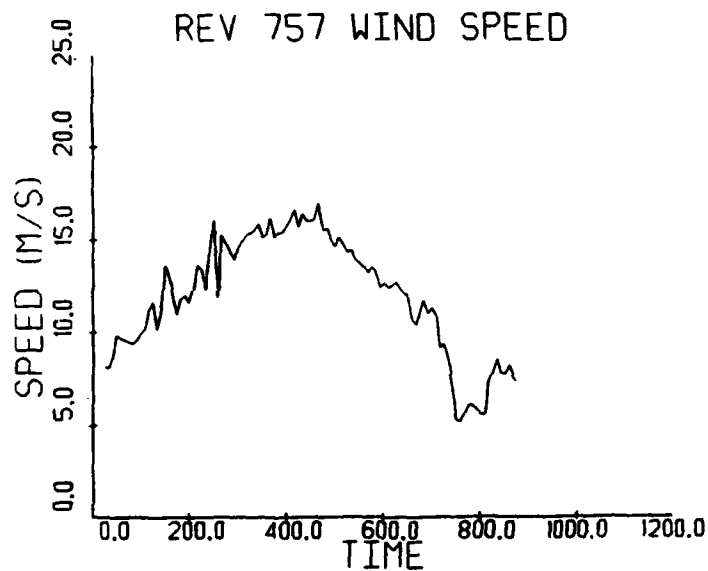
Figure 24. SASS-Derived Wind Conditions for
   Revolution 757

47
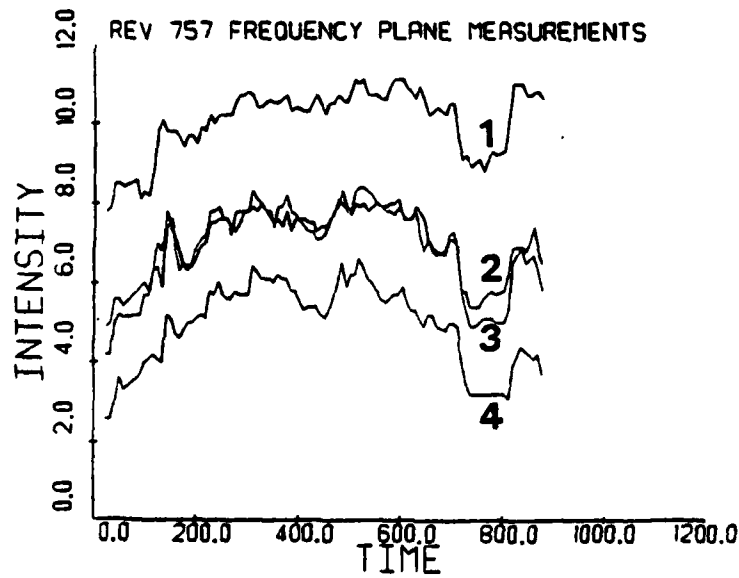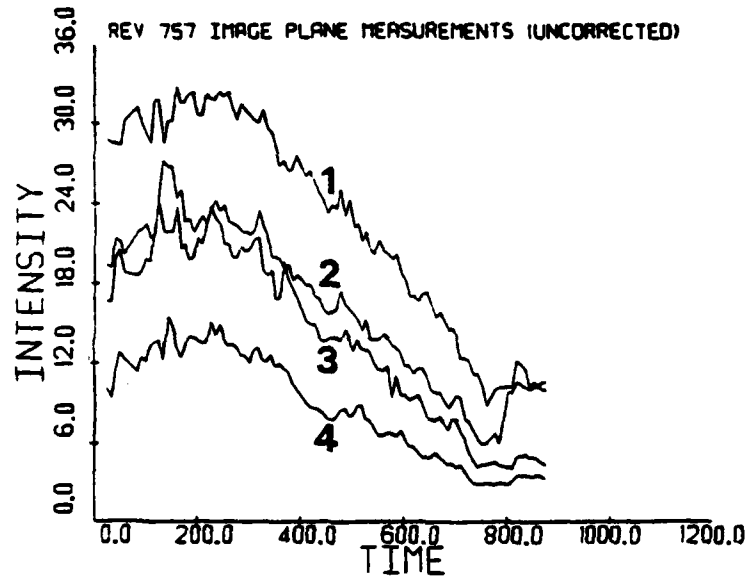
Figure 25.   Intensity Measurements Made at the Image and Frequency Planes of the SAR Optical Processor for Revolution 757

48

TABLE 5
OPTIMIZED MODEL PARAMETERS AND CORRELATION COEFFICIENTS
FOR REVOLUTION 757

Isotropic $(\alpha_1 = \alpha_2 = 0)$

	Image Plane Sub-Swath				Frequency Plane Sub-Swath			
	1	2	3	4	1	2	3	4
R	0.69	0.58	0.64	0.62	0.46	0.75	0.83	0.86
λ	0.95	0.79	1.2	1.0	0.14	0.32	0.48	0.62

Non-Isotropic

	Image Plane Sub-Swath				Frequency Plane Sub-Swath			
	1	2	3	4	1	2	3	4
R	0.82	0.73	0.75	0.71	0.82	0.86	0.89	0.91
γ	2.3	2.2	2.5	2.1	0.51	0.54	0.61	0.66
α_1	0.0	0.0	0.0	0.0	0.1	0.06	0.08	0.10
α_2	0.6	0.65	0.65	0.60	0.15	0.1	0.5	0.0

49

are somewhat larger than expected, particularly for the non-isotropic cases.

To correct the image plane measurements, a computer program was written which attempted to simulate the fall-off of image intensity due to a shifting of the Doppler spectrum as described in Section 3.2 and Appendix A. This program incorporated the modulation transfer function (MTF) of the signal film, the instantaneous Doppler central frequency and the frequency plane aperture size and location to calculate the relative fall-off of image intensity for a constant reflectivity scene as a function of time or distance along the pass. The original image plane measurements (Figure 25) were then divided by this correction. The correction for quarter swath 1 and the corrected image plane measurements for all four quarter swaths are shown plotted in Figure 26. Results of using this now rectified data to evaluate Eq. (3) are presented in Table 6. These results are encouraging; all correlations have increased substantially, and the wind speed exponents are now more consistent with our other data and the results of past investigations. The directional sensitivity is again seen to be small even though the wind direction changed over 180° between the start and end of the pass.

4.1.4 REVOLUTION 791

The SAR-derived wind data from 21 August 1978 collected during Revolution 791 are shown graphically in Figure 27 and are plotted in Figure 28. The wind speed is seen to range from about 5 to 12 m/s over the length of the pass, but vary only 5° in direction. The SAR measurements corresponding to these data are shown in Figure 29 for both image and frequency planes, all four quarter swaths. The agreement between the image plane, frequency plane and wind speed measurements is apparent. Results of evaluating Eq. (3) using these data are presented in Table 7. The correlations are high (0.79 - 0.94), and with the exception of quarter swath 1, the wind speed exponents

REV 757 IMAGE PLANE CORRECTION

REV 757 IMAGE PLANE MEASUREMENTS (CORRECTED)
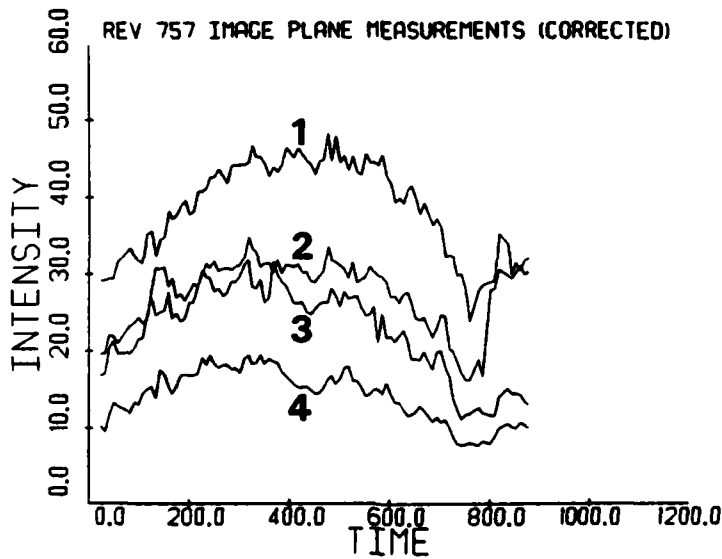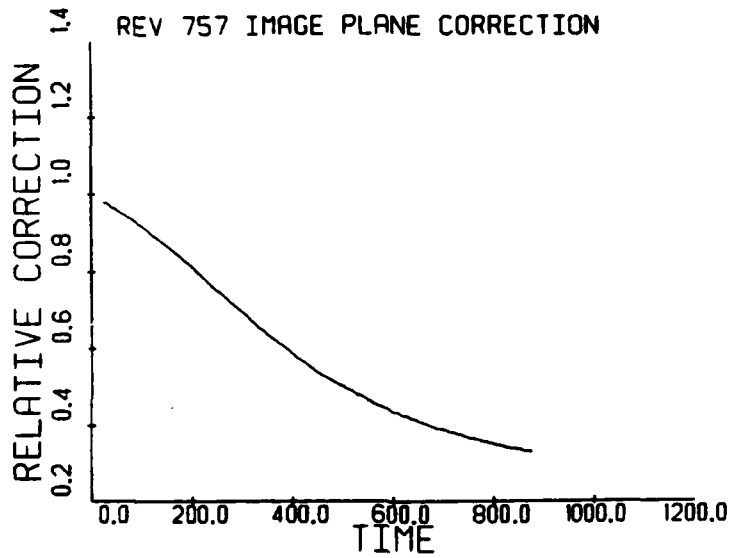
Figure 26. Theoretical Intensity Fall-Off Due to Doppler
Spectrum Shifting for Quarter Swath 1 and the
Corrected Image Plane Measurements From
Revolution 757

51

ΣERIM

TABLE 6
OPTIMIZED MODEL PARAMETERS AND CORRELATION
COEFFICIENTS FOR REVOLUTION 757 (Corrected)

	Isotropic ($\alpha_1 = \alpha_2 = 0$)			
	Image Plane Sub-Swath			
	1	2	3	4
R	0.89	0.69	0.90	0.85
γ	0.51	0.40	0.84	0.68

	Non-Isotropic			
	Image Plane Sub-Swath			
	1	2	3	4
R	0.89	0.79	0.90	0.85
γ	0.51	1.0	0.94	0.68
α_1	0.0	0.0	0.0	0.0
α_2	0.0	0.3	0.05	0.0
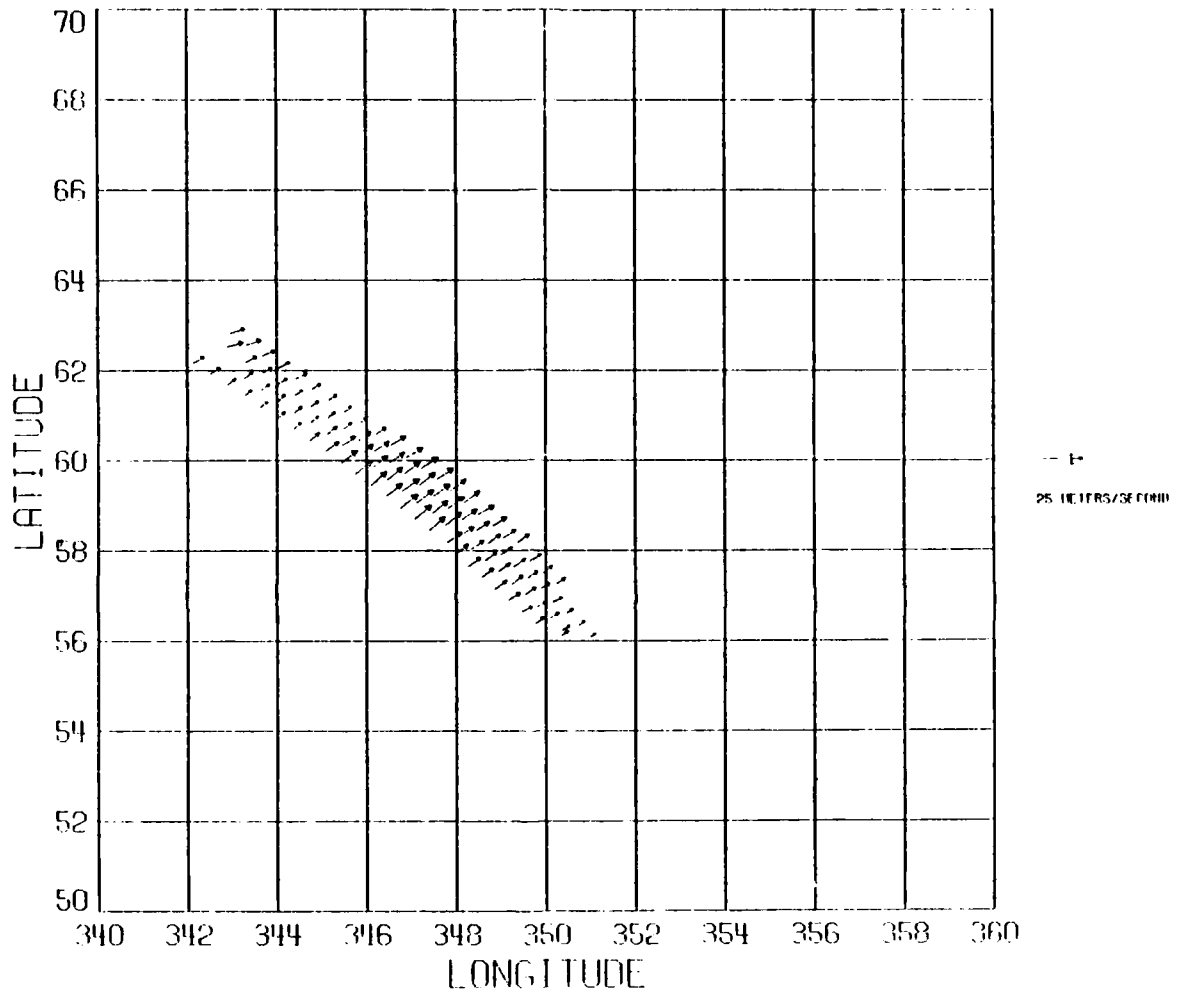
Figure 27. Graphical Depiction of SASS-Derived Winds for
Revolution 791
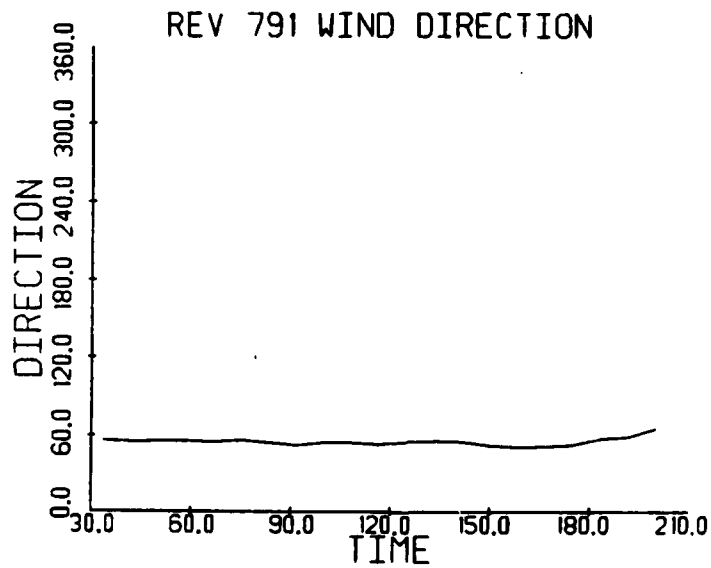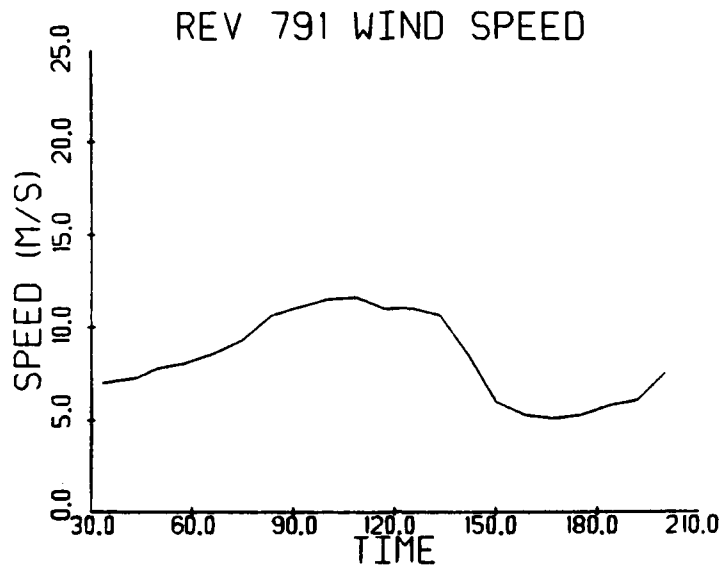
Figure 28.   SASS-Derived Wind Conditions for
                     Revolution 791
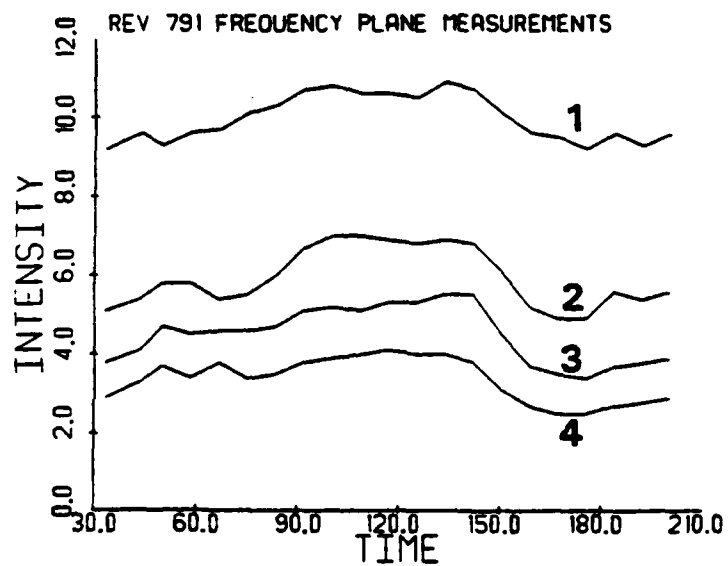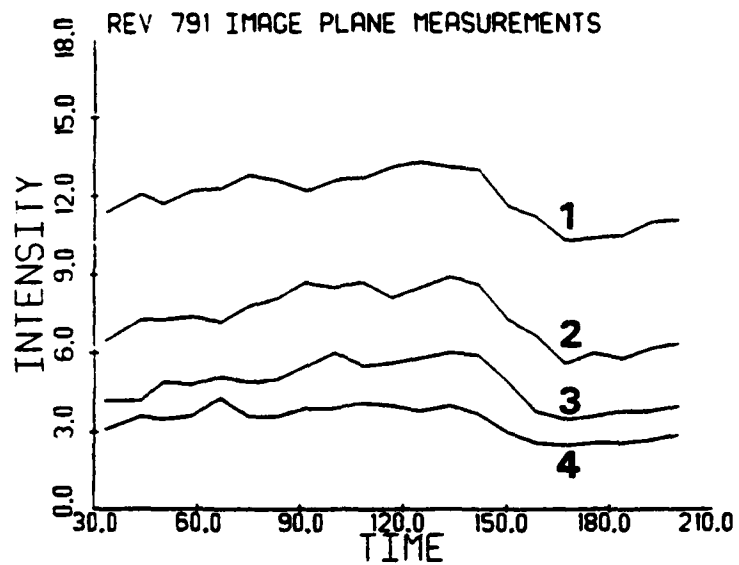
Figure 29. Intensity Measurements Made at the Image and
Frequency Planes of the SAR Optical Processor
for Revolution 791

TABLE 7
OPTIMIZED MODEL PARAMETERS AND CORRELATION COEFFICIENTS
FOR REVOLUTION 791

Isotropic ($\alpha_1 = \alpha_2 = 0$)

	Image Plane Sub-Swath					Frequency Plane Sub-Swath			
	1	2	3	4		1	2	3	4
R	0.94	0.90	0.86	0.79		0.81	0.81	0.87	0.81
γ	0.24	0.44	0.57	0.57		0.15	0.34	0.49	0.48

Non-Isotropic

	Image Plane Sub-Swath					Frequency Plane Sub-Swath			
	1	2	3	4		1	2	3	4
R	0.94	0.94	0.87	0.83		0.81	0.83	0.87	0.84
γ	0.23	0.45	0.56	0.49		0.15	0.35	0.49	0.47
α_1	0.0	0.0	0.18	0.2		0.1	0.0	0.0	0.14
α_2	0.4	0.8	0.8	0.8		0.0	0.55	0.45	0.8

56

all lie between 0.3 and 0.6. Although some of the optimized α_1 and α_2 coefficients seem large, they have a negligible effect on the correlations due to the small change in wind direction for this data set.

4.1.5 DISCUSSION OF RESULTS

In this section of the report, a discussion of the results of the above analysis is presented. Included in this discussion is an inter-comparison of the results for each revolution, as well as a comparison of the results with those of previous investigations.

Presented in Figures 30 and 31 are graphs of the correlation co-efficients (R) plotted against the wind speed exponents from three revolutions, all four quarter swaths, for the image and frequency plane measurements, respectively. The results from Revolution 547 are not included in this or the following plots because of the apparent presence of non-wind related surface features in this data set. The results shown in Figures 30 and 31 were obtained assuming the scattering is isotropic (i.e., $\alpha_1 = \alpha_2 = 0$). Also shown on the plots are the mean and standard deviation of the wind speed exponents displayed as error bars. Examination of Figures 30 and 31 reveals many similarities. In both cases, the correlations are seen to generally lie between 0.8 and 0.9 with few exceptions. In addition, the wind speed exponents generally increase from quarter swath 1 to quarter swath 4 for both cases. The fact that the wind speed exponents change from quarter swath-to-quarter swath will be discussed further in Section 4.3.

Presented in Figures 32 and 33 are similar plots to Figures 30 and 31 except they are for the non-isotropic cases, image and frequency measurements, respectively. These were produced assuming the data behaved non-isotropically, that is, α_1 and α_2 in Eq. (3)
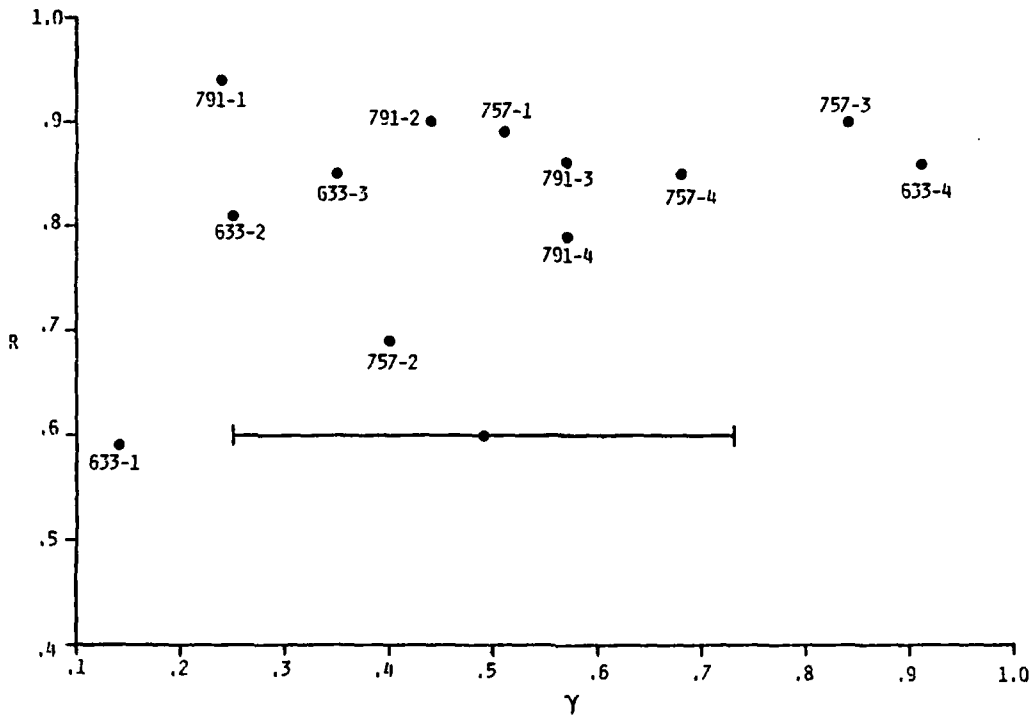
Figure 30. Correlation Coefficients (R) vs. Wind Speed Exponents (γ) for Image Plane Measurements Assuming Isotropic Behavior
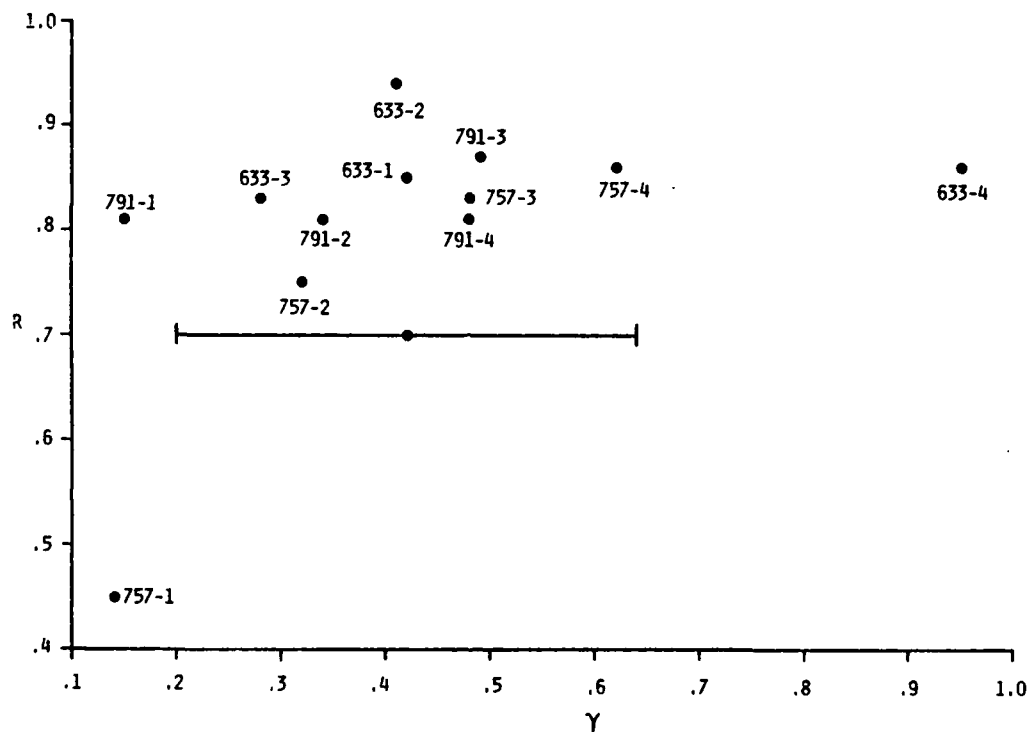
Figure 31. Correlation Coefficients (R) vs. Wind Speed Exponents (γ) for Frequency Plane Measurements Assuming Non-Isotropic Behavior

59
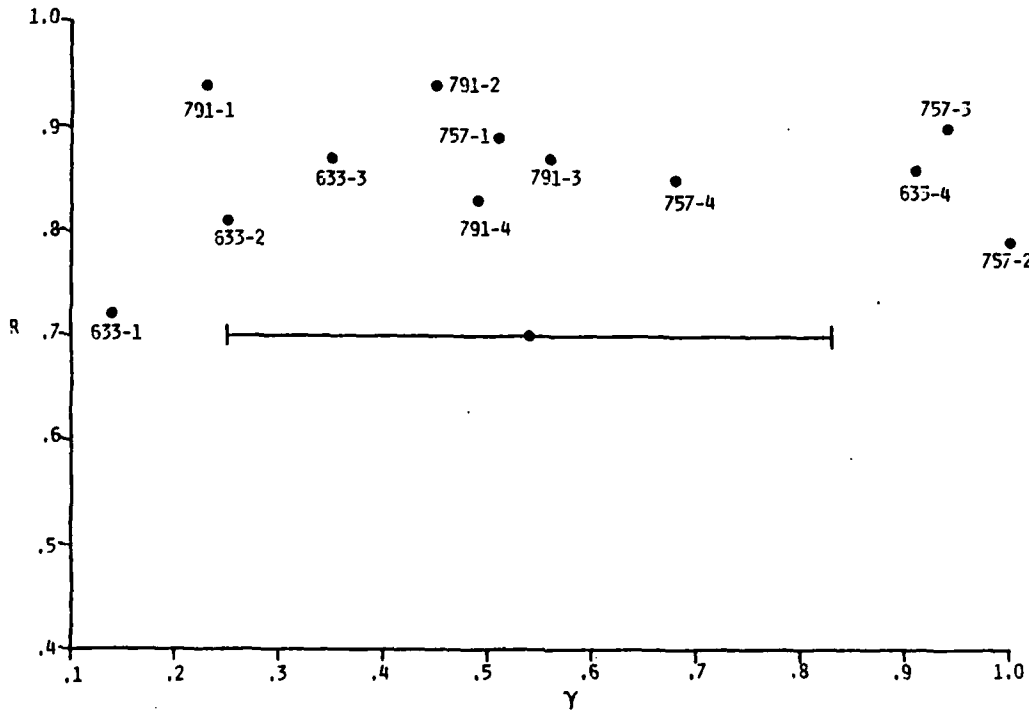
Figure 32.   Correlation Coefficients (R) vs. Wind Speed Exponents (γ) for Image Plane Measurements Assuming Non-Isotropic Behavior

60
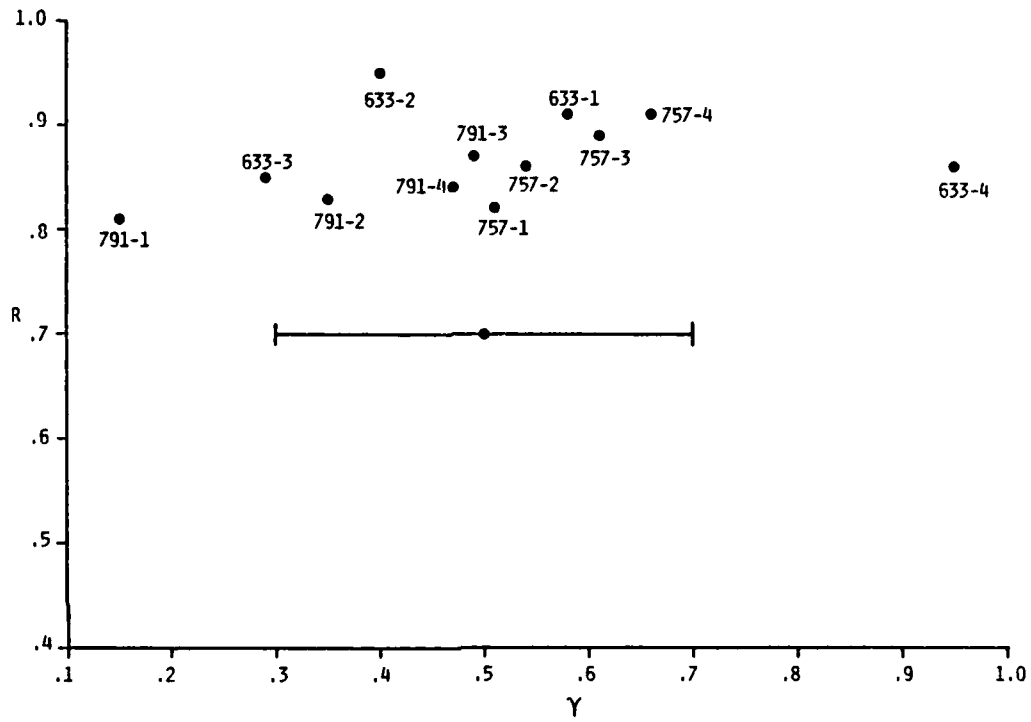
Figure 33.   Correlation Coefficients (R) vs. Wind Speed Exponents (γ) for Frequency Plane Measurements Assuming Non-Isotropic Behavior

were allowed to vary in order to maximize the correlation coeffi-
cients. Again, these both appear very similar. The correlations
have improved slightly and now lie between 0.8 and 1.0 with very few
exceptions. The mean wind speed exponents also increase from quarter
swath 1 to quarter swath 4 for both cases. The deviations of the
wind speed exponents have increased significantly for the image plane
measurements, but have remained nearly constant for the frequency
plane measurements. There is no apparent correlation between the R
and γ values plotted in these figures, except that the lowest R al-
ways corresponds to the smallest value of γ. It is also interesting
to note that these values are also all from quarter swath 1, indi-
cating that optimum results are obtained at larger incidence angles.

Presented in Figures 34 and 35 are graphs of the change in cor-
relation coefficient (ΔR) plotted against the values of the aniso-
tropic coefficients (α_1 and α_2) for the optimized cases, image
and frequency plane measurements, respectively. Again the two plots
appear very similar. With the exception of Revolution 757, quarter
swath 1, the correlations increase less than 0.15, and in fact, most
cases show little or no (<0.01) improvement even when optimization
of the model resulted in large anisotropic coefficients.

When results of this study are compared with those of previous
investigators, many of the same general conclusions can be reached.
The Seasat SAR L-band data behaves very nearly isotropically and is
related to wind speed through a simple power law relationship. Com-
parison of wind speed exponents from the different investigations
show some differences. In the study by Jones, et al. (1981), a wind
speed exponent of 0.4 was obtained from an analysis of quarter swath
4 data. Our analysis has indicated that a wind speed exponent of
0.7 is more appropriate for quarter swath 4. The 0.7 value also
agrees more closely with theory as will be discussed in Section 4.3.
This discrepancy could be due to the use of image film products in

62
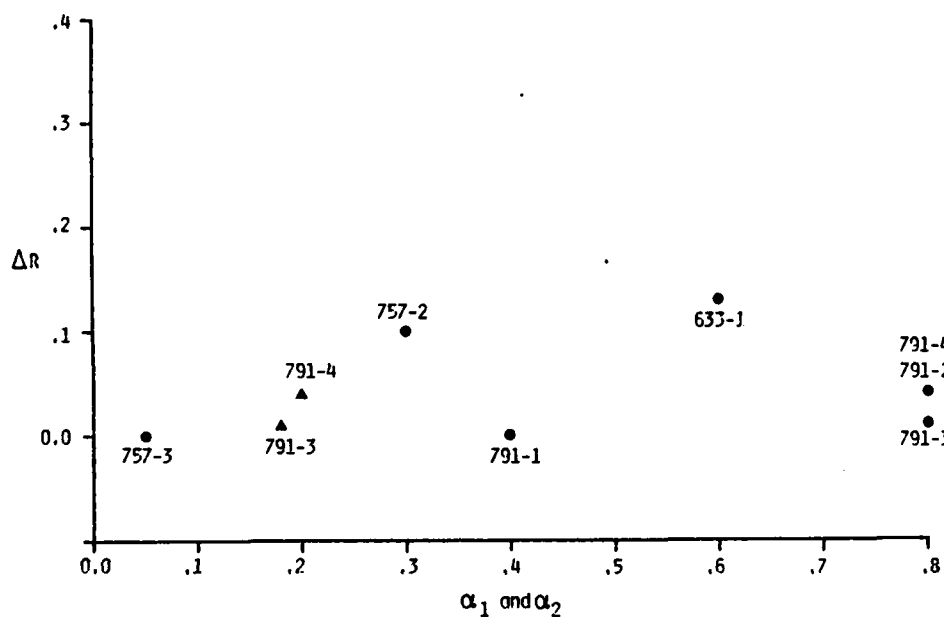
Figure 34. Change in Correlation Coefficient (ΔR) vs. Anisotropic
Coefficients α_1 (▲) and α_2 (●) of Optimized Model
Results Using Image Plane Measurements
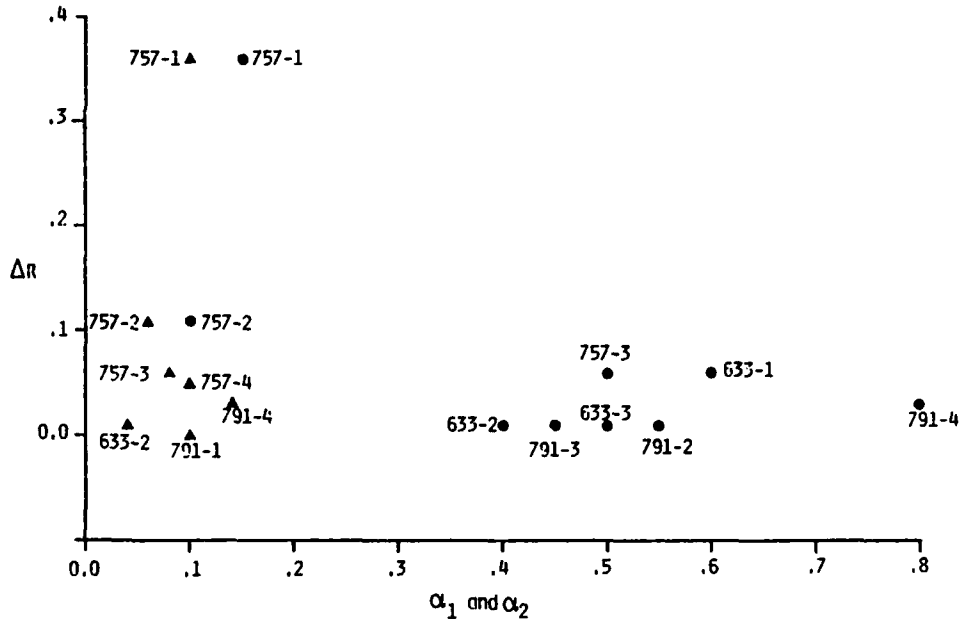
Figure 35.   Change in Correlation Coefficient (ΔR) vs. Anisotropic
Coefficients α_1 (▲) and α_2 (●) of Optimized Model
Results Using Frequency Plane Measurements

the Jones study, or that Doppler shifting was not accounted for. In the analysis of Thompson, et al. (1981), wind speed exponents of 0.5 ±0.1 were obtained, which agree more closely with our results. However, Doppler shifting was not accounted for in the study of Thompson, et al. (1981), and it seems likely that their results could be improved by including these effects, for example in the Revolution 1255 data shown in Figure 5 of this report.

4.2 WIND SPEED PREDICTIONS

The analysis presented thus far has included only an evaluation of the model presented in Eq. (2). This study has shown that on a revolution-to-revolution basis, given sufficient wind speed, SAR backscatter intensity measurements can be successfully correlated to SASS-derived surface wind speed. Now we attempt to use the SAR-measured backscatter intensities to predict wind speed and evaluate the accuracy of the technique. Using data from quarter swath 3 of Revolution 757, wind speeds were predicted from both image and frequency plane measurements. The assumption was made that the wind speed was known at a single point approximately halfway through the pass. In other words, the SASS-derived and SAR-calculated wind speeds normalized to this single point observation. The results of these calculations are shown in Figures 36 and 37 for the image and frequency plane measurements, respectively. Scatterplot representations of these results are alternatively shown in Figures 38 and 39 again for the image and frequency plane measurements, respectively. The rms error for these predictions are 1.8 and 2.2 m/s for the image and frequency plane measurements, respectively. The distribution of these errors is shown plotted in Figures 40 and 41 for the image and frequency plane cases, respectively. Also shown on these figures are the appropriate normal distributions given the mean and standard deviation of the errors for each case. The nonzero means are due to truncation errors. In neither case are the errors distributed very

65
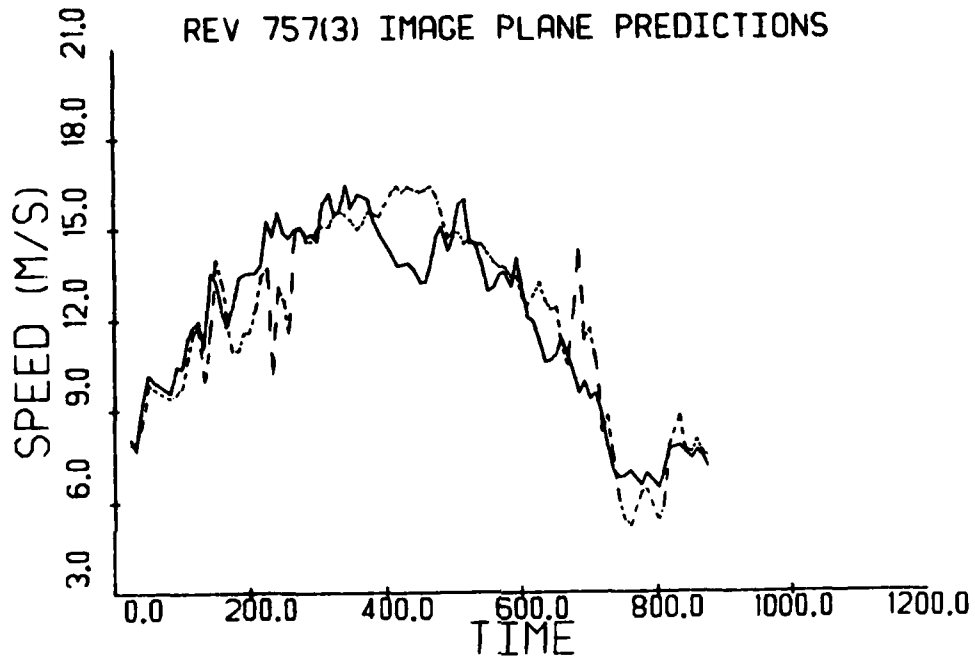
Figure 36.   SAR-Derived (Solid) and SASS-Derived (Dashed)
            Wind Speeds for Image Plane Measurements from
            Revolution 757, Quarter Swath 3
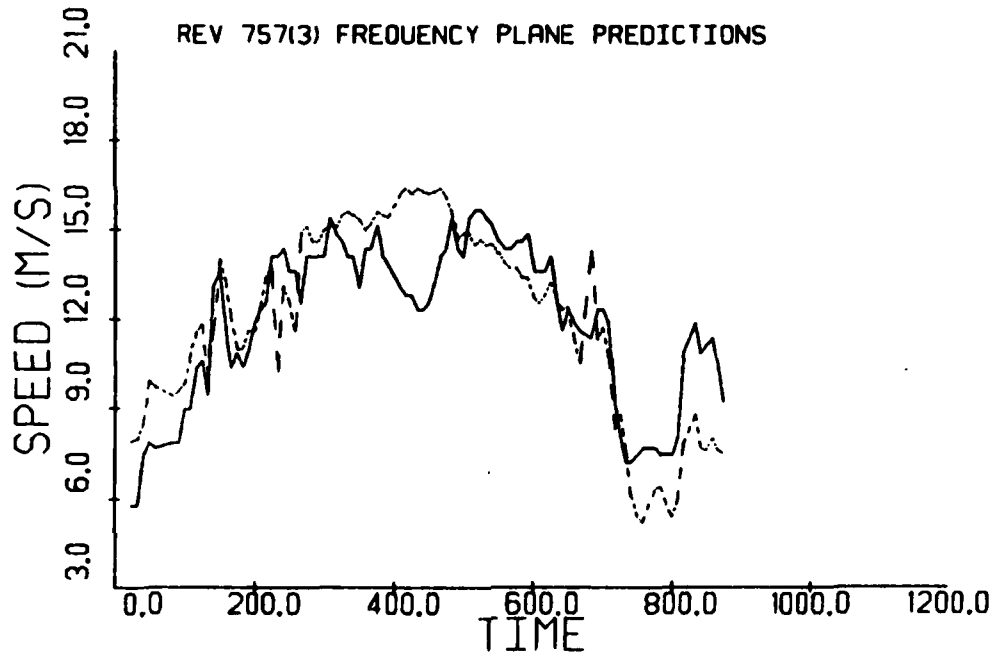
Figure 37.   SAR-Derived (Solid) and SASS-Derived (Dashed) Wind
             Speeds for Frequency Plane Measurements from
             Revolution 757, Quarter Swath 3
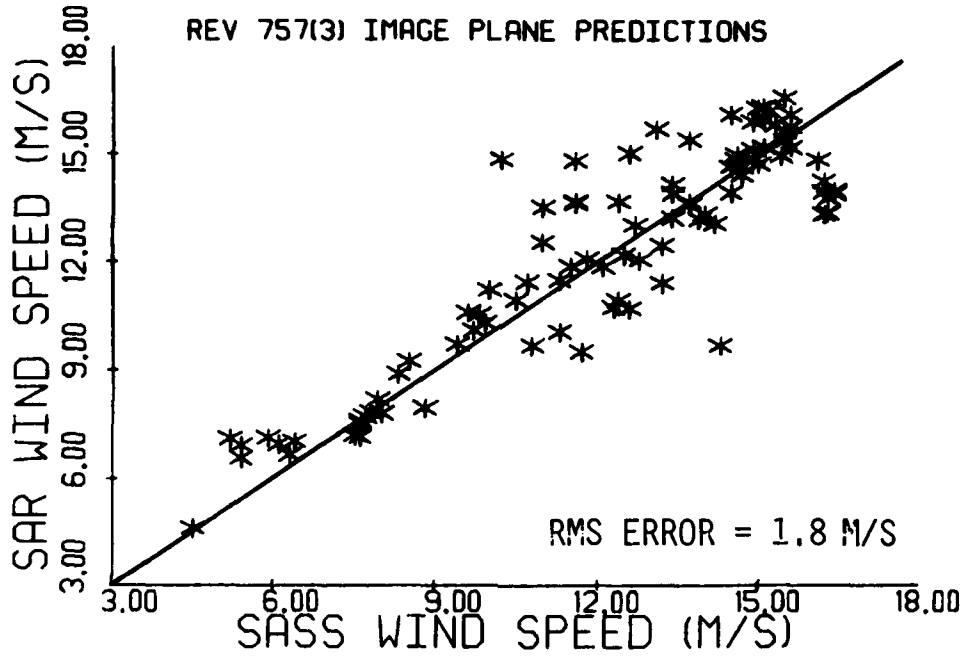
Figure 38. Scatterplot of SAR-Derived vs. SASS-Derived
Wind Speeds for Image Plane Measurements from
Revolution 757, Quarter Swath 3
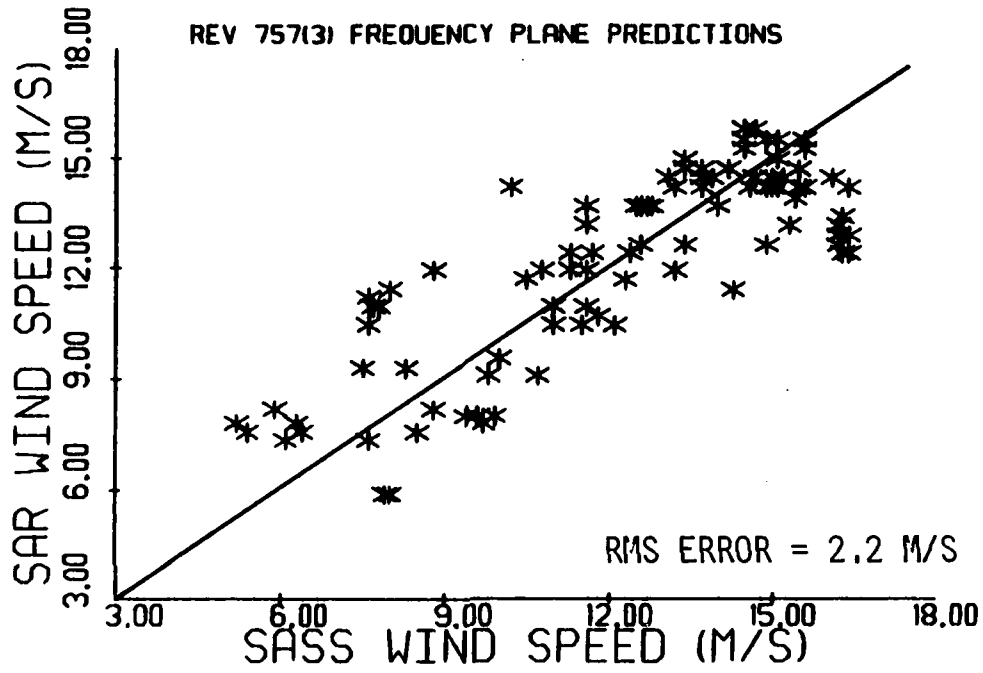
Figure 39. Scatterplot of SAR-Derived vs. SASS-Derived Wind
Speeds for Frequency Plane Measurements from
Revolution 757, Quarter Swath 3
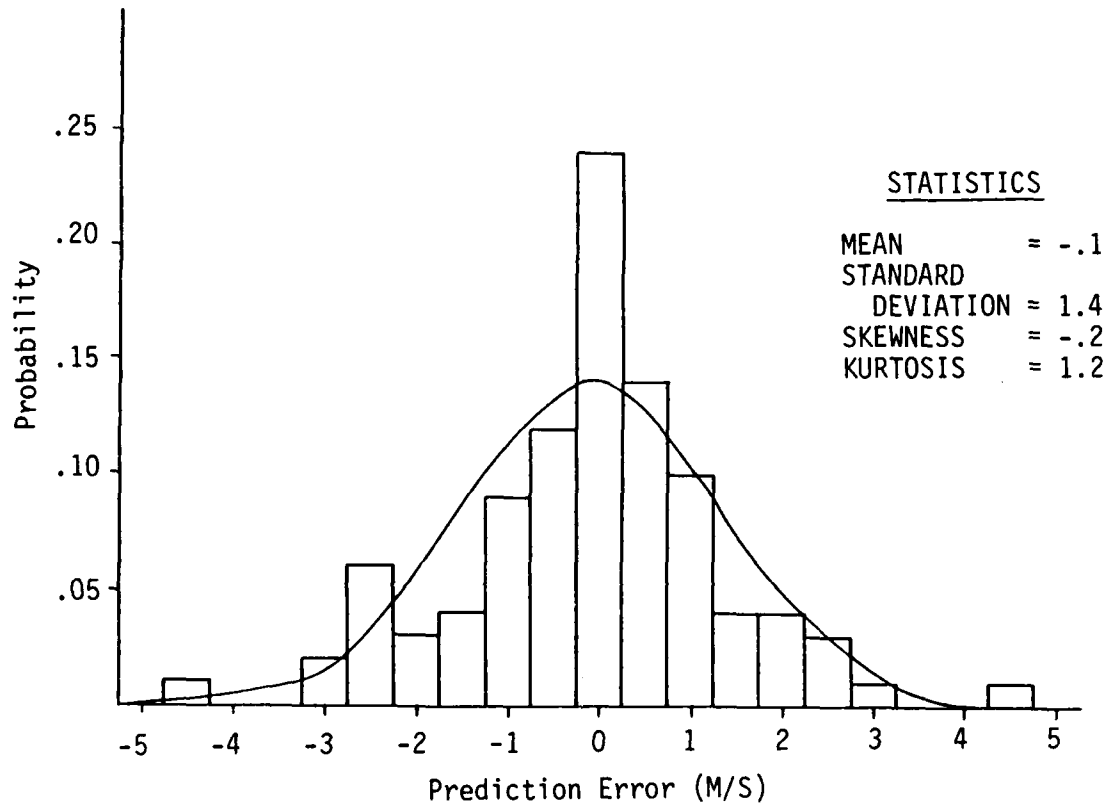
Figure 40. Distribution of Errors in SAR-Derived Wind Speed
           Predictions for Image Plane Measurements from
   Revolution 757, Quarter Swath 3
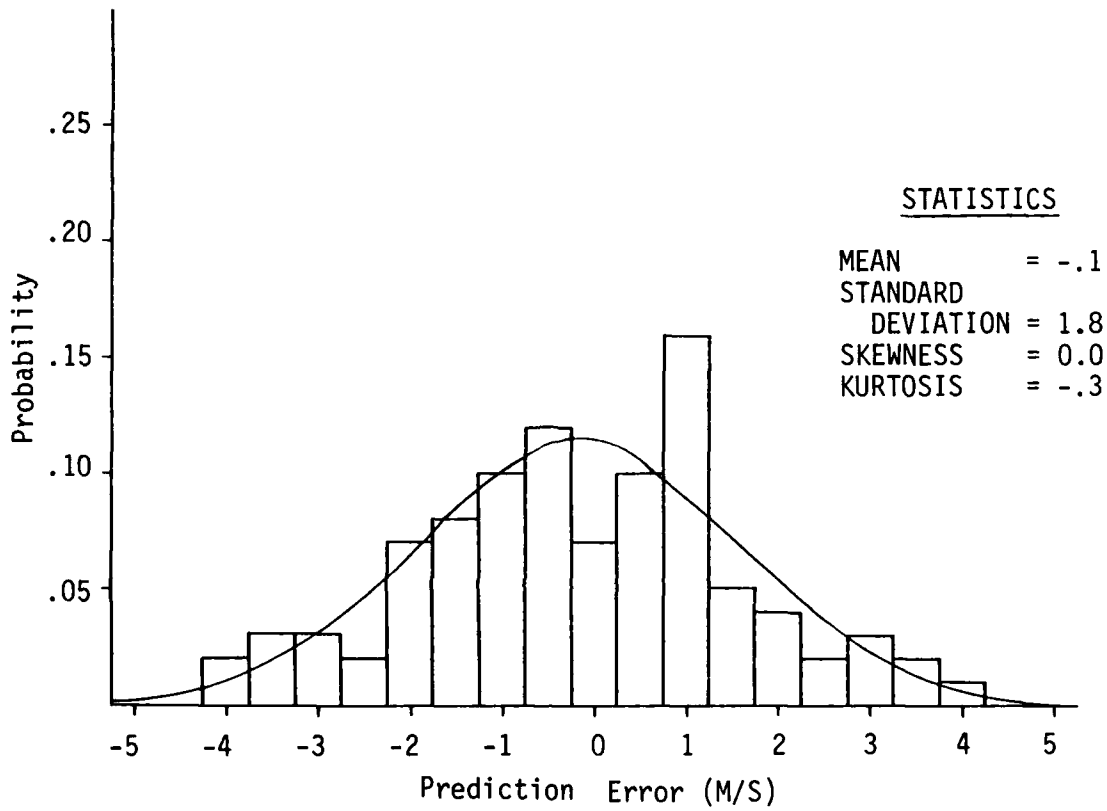
Figure 41. Distribution of Errors in SAR-Derived Wind
Speed Predictions for Frequency Plane
Measurements from Revolution 757, Quarter
Swath 3

different from normal, although the image plane errors do have a relatively large kurtosis, indicating a large percentage of accurate predictions.

These results were obtained using the regression coefficients for Revolution 757. Since there is some variability in these co-efficients from pass to pass, a somewhat poorer prediction would be expected using calibration data from a different pass. For example, if the wind speed exponents from all the data presented in this paper were averaged together and applied to Revolution 757, the rms error in the predicted wind speed would be approximately 3 m/s for both the image and frequency plane measurements.

4.3 THEORETICAL CONSIDERATIONS

The variation in the radar cross section of the ocean surface with wind speed is theoretically investigated in this section using the composite surface scattering model developed by Wright (1968) and Valenzuela (1978). In this model, the surface is assumed to be made up of a large number of randomly oriented patches. The Bragg scattering cross section of each patch is calculated using the local incidence angle, and the results are summed incoherently to obtain the total (average) cross section. The slopes of the patches are assumed to be normally distributed with mean zero and standard deviation S. In practice, the summation is carried out over slopes up to three times this standard deviation. Patches which are oriented at angles less than $10°$ from the specular direction are ignored in this summation, since the Bragg scattering mechanism breaks down for such orientations.

The standard deviation, or rms slope, S is related to the wind speed U through the empirical formula

$$S^2 = 0.004 + 0.00081 \ U \qquad (4)$$

obtained by Cox and Munk (1954). A similar relationship can be derived by integrating the Phillips spectrum over wavelengths from approximately 10 times the Bragg wavelength to the maximum surface wavelength for a given wind speed. The normalized radar cross section, σ_0, was calculated from the composite model as a function of wind speed using Eq. (4). The results are plotted in Figure 42 for two incidence angles (20° and 25°) typical of Seasat quarter swaths 1 and 4.

The slopes of the lines in Figure 42 are close to the values of γ obtained from the analysis of the Seasat data presented in the previous section. Note also that the slope for an incidence angle of 25° (quarter swath 4) is larger than that for an incidence angle of 20° (quarter swath 1), as observed in the actual data. This model also predicts a difference in the average σ_0 from quarter swath 1 to quarter swath 4 of 3–5 dB, which is not unreasonable although it is somewhat larger than most measurements using Seasat data.

In summary, although the agreement is not perfect, the results of this model are encouragingly close to the Seasat observations. Therefore, it seems probable that the dominant mechanism for the windspeed dependence of σ_0 in this range of incidence angles is the variation in the rms slope of the surface. Additional variability may be caused by the formation of breaking waves at higher wind speeds. The radar cross section of breaking waves is not included in the formulation of the composite model used in this study.
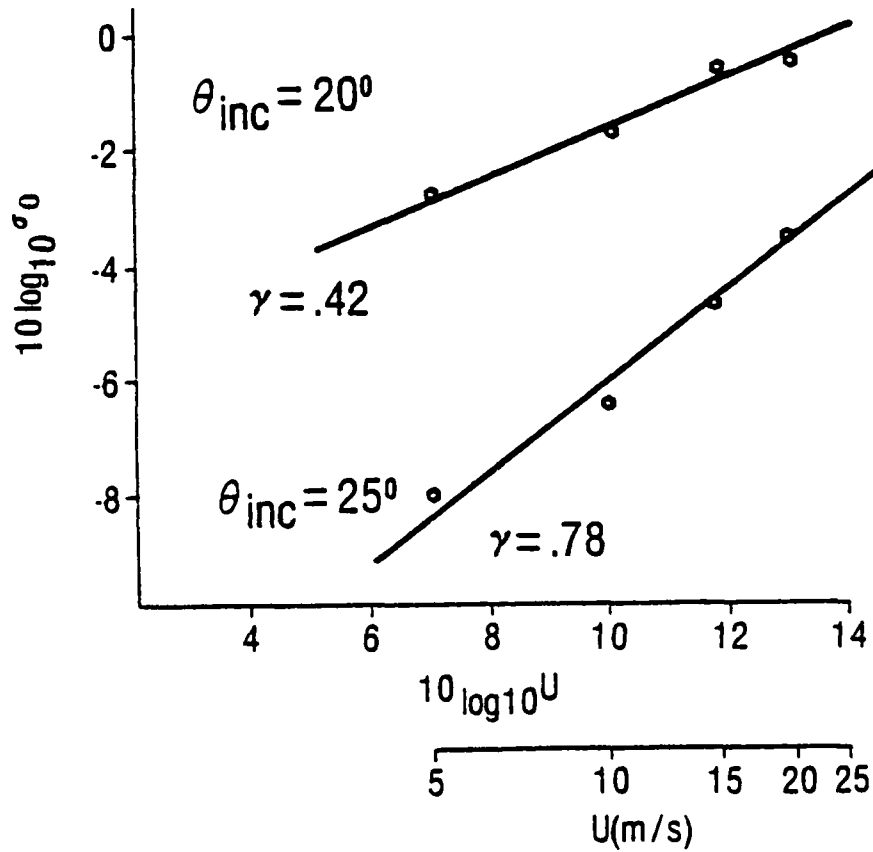
Figure 42. Theoretical L-Band Radar Cross Section Predictions
Based on Composite Scattering Theory for a Range
of Wind Speeds at 20° and 25° Incidence Angle

74

5
CONCLUSIONS AND RECOMMENDATIONS

This report has evaluated the use of Seasat SAR intensity measurements for ocean surface wind determination. This study included: (1) a brief review of microwave scattering from the ocean surface, (2) a review of past work by other investigators on using Seasat SAR data for wind measurements, (3) a discussion of the various SAR system parameters that can affect wind measurements, (4) the evaluation of an empirical model which relates radar backscatter to ocean surface winds, and (5) a comparison of our empirical results with those predicted by composite scattering theory.

Results obtained from this study include:

1. Seasat SAR backscatter measurements made from image film may in some cases exhibit errors due to the non-linear nature of the backscatter extraction technique.

2. Seasat SAR backscatter measurements change with along-track distance independently of surface scattering properties due to shifting of the Doppler spectrum.

3. Correction of Doppler spectrum shifting effects and development of a simplified measurement technique allowed utilization of longer passes of data than past Seasat SAR wind studies.

4. An empirical model relates Seasat SAR backscatter to ocean surface wind conditions, yielding results consistent with past investigators, and apparently having smaller systematic errors.

5. Predictions based on composite surface scattering theory behaved similarly to empirical results.

In summary, this study indicated that the backscatter of Seasat SAR data is dependent on ocean surface wind speed. Results also indicate that to a first order, the L-band SAR data collected by Seasat behaves isotropically. This should be further verified through examination of scatterometer data collected at the same frequency. Additional work is clearly warranted if Seasat-type SAR data is to be fully exploited for wind information. However, benefits such as the capability of studying mesoscale variations in wind speed are at least conceivable using SAR data.

Future work in this area should investigate the higher order statistics of the SAR data as well as, possibly, spatial patterns of reflectivity in the imagery. Results of this study, and others before it, indicate that Seasat SAR backscatter measurements contain information only on wind speed and not direction. A recent study by Longuet-Huggins (1982), has indicated that the skewness of sea surface slopes is related to wind speed and the angle between the wind direction and the direction of long wave propagation. This relationship may also manifest itself in Seasat SAR imagery. Often, spatial patterns or texture effects may be present due to locally wind-generated seas or phenomena such as wind rows, which could be imaged by high resolution SAR systems.

It is recommended that future work study the image statistics of digitally-processed Seasat SAR imagery collected over a variety of surface conditions. These data should be chosen so as to contain at least one (preferably two or more) NOAA data buoy operating at or near the time of the satellite overpass. The use of higher-order statistics or image textural measures may lead to the development of a multi-parameter model which allows the determination of both wind speed and direction directly from SAR imagery.

APPENDIX A
RADIOMETRIC EFFECTS OF DOPPLER SPECTRUM VARIATIONS

APPENDIX A
RADIOMETRIC EFFECTS OF DOPPLER SPECTRUM VARIATIONS

The along-track radiometric stability of the Seasat SAR is an issue of concern to those attempting to correlate the SAR image intensity with geophysical parameters, such as winds, over large areas. The analysis described in this Appendix deals with one aspect of this problem, namely the effect of Doppler spectrum variations on the radiometric properties of the SAR image. The discussion is in the context of optically processed imagery since the ability of optical methods to process long swaths in a continuous manner makes these methods attractive for this application. The effects of Doppler spectrum "wandering" on digitally processed data must also be considered when comparing successive frames of imagery, using methods similar to those described here.

A.1 BACKGROUND

The azimuth, or Doppler, spectrum of the signals received by a SAR is dependent on the antenna gain pattern, the antenna look direction, the platform velocity, and the radial velocity of the objects in the scene. For Seasat, the received Doppler spectrum has a width of about 900 Hz. Because this spectrum is, in effect, sampled at the pulse repetition frequency (PRF) the actual spectrum is not distinguishable from a set of "alias" spectra separated in frequency by multiples of the PRF. Approximating the antenna gain pattern by a Gaussian function, the received signal spectrum can be written as

$$S_i(f) = \sigma_0 \sum_{n=-}^{\infty} \exp\left\{-2.77\left(\frac{f - f_c - nf_r}{B}\right)^2\right\} \qquad (A-1)$$

where σ_0 is the radar cross section of the surface, $B = 900$ Hz is the 3 dB bandwidth of the Doppler spectrum, f_c is the peak frequency, and $f_r = 1647$ Hz is the pulse repetition frequency (PRF).

When this signal is recorded on film, the higher frequencies are attenuated, or recorded with less efficiency than the lower frequencies. This effect is described by the modulation transfer function (MTF) of the recording system. Measurements in the optical processor indicate that the shape of the MTF can be approximated by the sum of a Gaussian and an exponential function, i.e.,

$$M(f) = \frac{1}{2} e^{-\left(\frac{f}{B_r}\right)^2} + \frac{1}{2} e^{-\left|\frac{f}{B_r}\right|} \tag{A-2}$$

where B_r = 600 Hz is the system bandwidth. Thus, the spectrum of the signals recorded on the signal film (as measured in the optical processor) is given by

$$S_o(f) = M(f)S_i(f) + N(f) \tag{A-3}$$

where $N(f)$ is the noise spectrum, which has approximately the same shape as the MTF. Examples of measured spectra for Seasat Rev. 757 are shown in Figures A-1 through A-5. Note that the effects of the MTF are clearly visible in these measurements, causing the alias spectra to be of unequal amplitude and the peak frequencies to be separated by less than the PRF. Note also that the peak frequencies vary as a function of the distance along the swath during this pass. The implications of this spectrum shift for the radiometric calibration of the data will be discussed in Section A.3.

A.2 DOPPLER SPECTRUM MEASUREMENTS

In order to measure the spectral shifts during Rev. 757, the spectra shown in Figures A-1 through A-5 were divided by the MTF. Using the measured MTF, the data appeared to be over-corrected, as indicated by the amplitudes and separation of the real and alias spectra. Using a modified MTF of the same form as Eq. (A-2) but with B_r = 900 Hz, a better correction was obtained. The corrected

Figure A-1. Area A
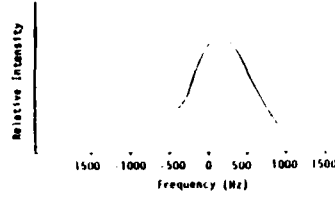


Figure A-2. Area B
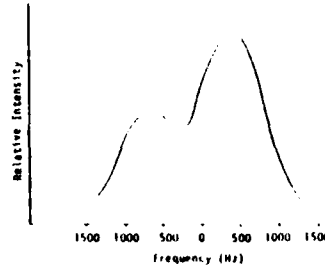

Figure A-3. Area C
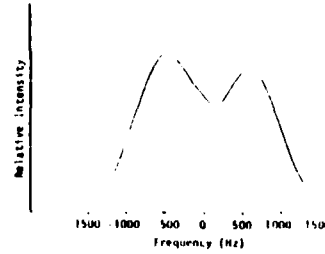
Figure A-4. Area D
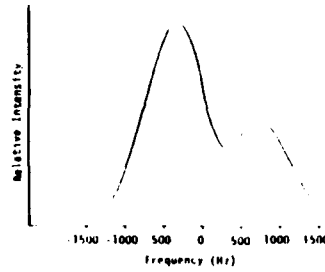
Figure A-5. Area E
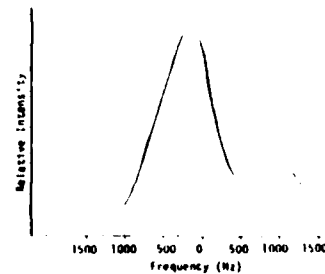
MEASURED DOPPLER SPECTRUM

spectra using this MTF are shown in Figures A-6 through A-10, and the peak frequencies of the real and alias spectra are shown in Table A-1.

Shifts in the peak frequency of the Doppler spectrum along the swath are due to earth rotation effects and spacecraft attitude variations. The Doppler shift due to the earth's rotation is given by

$$\Delta f_c = - \frac{2\Omega R_e}{\lambda} \cos (L) \sin \phi \sin \Theta \qquad (A-4)$$

where Ω is the earth's angular velocity (7.272×10^{-5} rad/s), R_e is the earth's radius (~6370 km), λ is the radar wavelength (23.5 cm), L is the latitude, ϕ is the radar look direction (from North), and Θ is the incidence angle (~20°).

The Doppler shift due to spacecraft attitude variations is given approximately by

$$\Delta f_c = \frac{2V}{\lambda} (\cos \Theta \sin P - \sin \Theta \sin Y) \qquad (A-5)$$

where V is the swath velocity (nominally 6800 m/s), P is the pitch angle, and Y is the yaw angle. P is positive for nose-up rotations of the spacecraft and Y is positive for clockwise rotations (looking down). These angles are given in the auxiliary data listing for the Seasat pass under consideration.

The latitude variation and changes in pitch and yaw for a portion of Rev. 757 are shown in Figure A-11. Also shown in this figure are the calculated Doppler shifts due to the earth's rotation and the changes in spacecraft attitude along the pass. The total Doppler shift is shown in Figure A-12, along with the peak frequencies obtained from the optical processor measurements. Note that the trend is predicted quite well by the above equations. There is an offset of about 200 Hz between the calculated and observed Doppler frequencies, but this is to be expected since there are Doppler shifts

82

ΣERIM

INPUT SIGNAL − 20 m from end
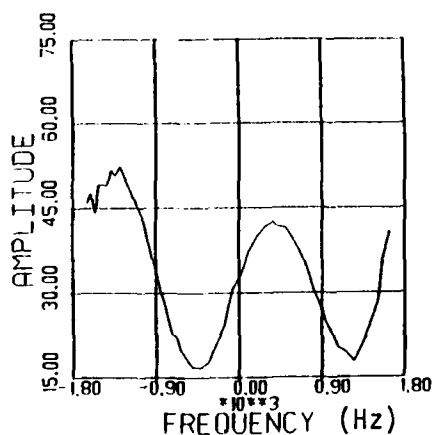
Figure A-6. Corrected Doppler
Spectrum for Area A,
Rev. 757

INPUT SIGNAL − 15 m from end
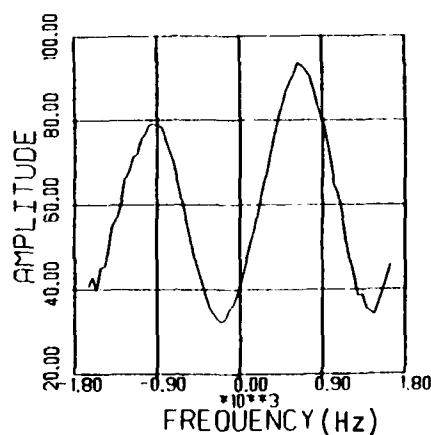

Figure A-7. Corrected Doppler
Spectrum for Area B,
Rev. 757

INPUT SIGNAL − 10 m from end
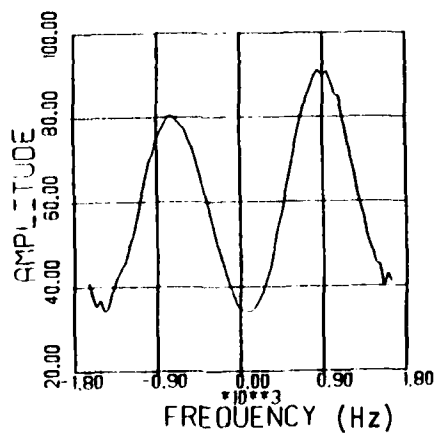
Figure A-8. Corrected Doppler
Spectrum for Area C,
Rev. 757

83

INPUT SIGNAL – 5 m from end
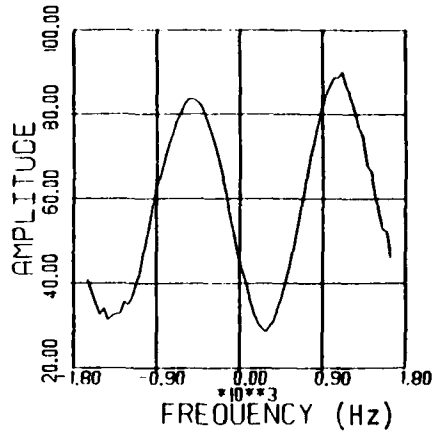
Figure A-9. Corrected Doppler Spectrum for Area D, Rev. 757

INPUT SIGNAL – end of pass
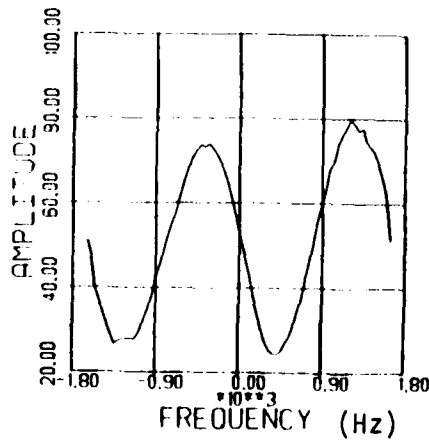
Figure A-10. Corrected Doppler Spectrum for Area E, Rev. 757

TABLE A-1
DOPPLER PEAK FREQUENCIES MEASURED FOR REV. 757

Location	Time	f_c (actual spectrum)	f_c (alias spectrum)
A	22:37:36	400 Hz	-1300 Hz
B	22:40:13	700 Hz	- 950 Hz
C	22:42:49	900 Hz	- 730 Hz
D	22:45:25	1050 Hz	- 500 Hz
E	22:48:01	1250 Hz	- 400 Hz
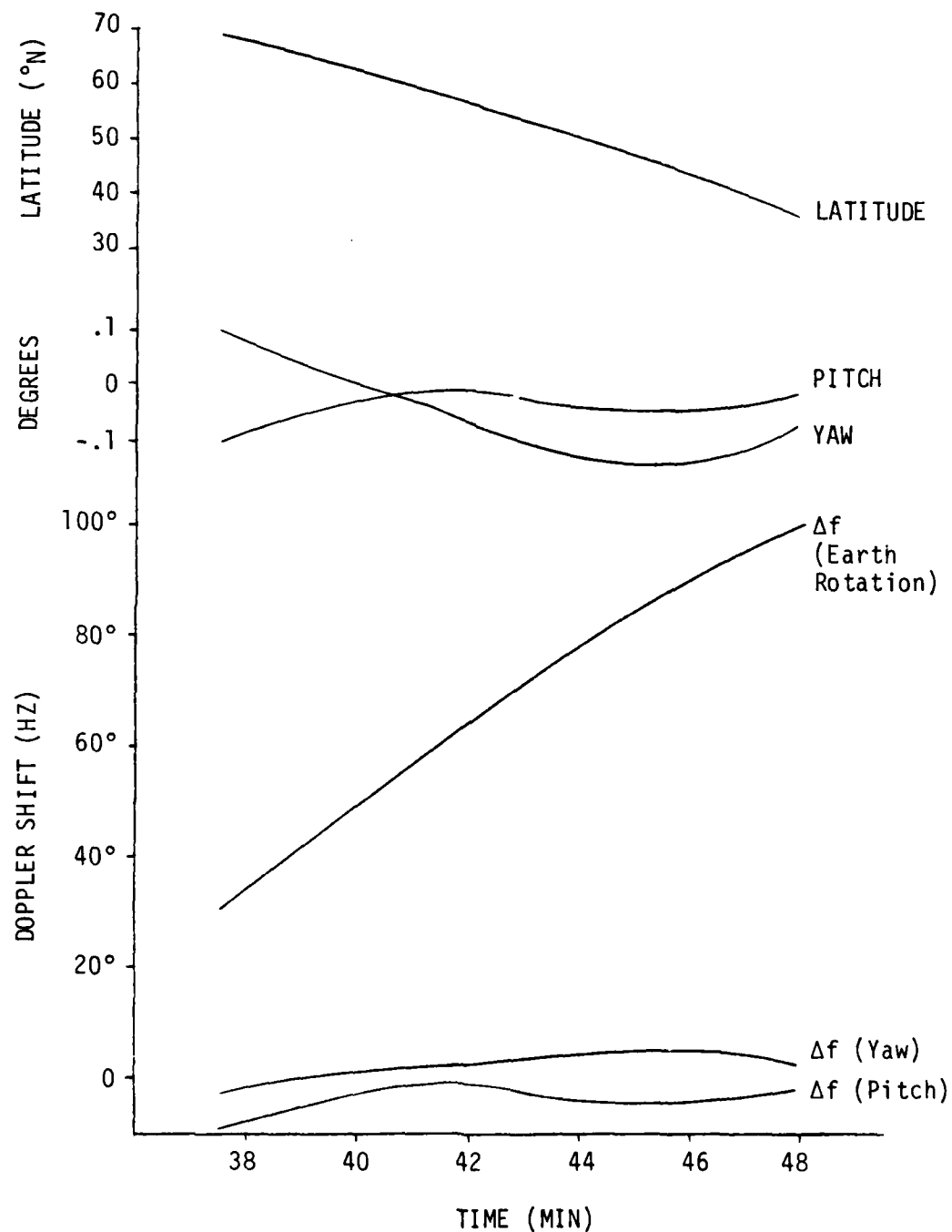
Figure A-11.   Seasat Orbital Parameters and Associated Doppler Shifts
                for Rev. 757
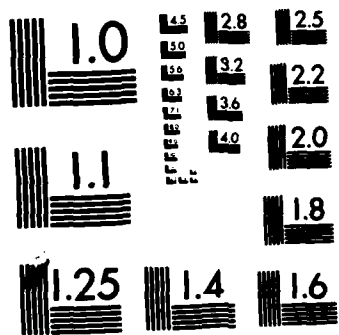
MICROCOPY RESOLUTION TEST CHART

NATIONAL BUREAU OF STANDARDS-1963-A
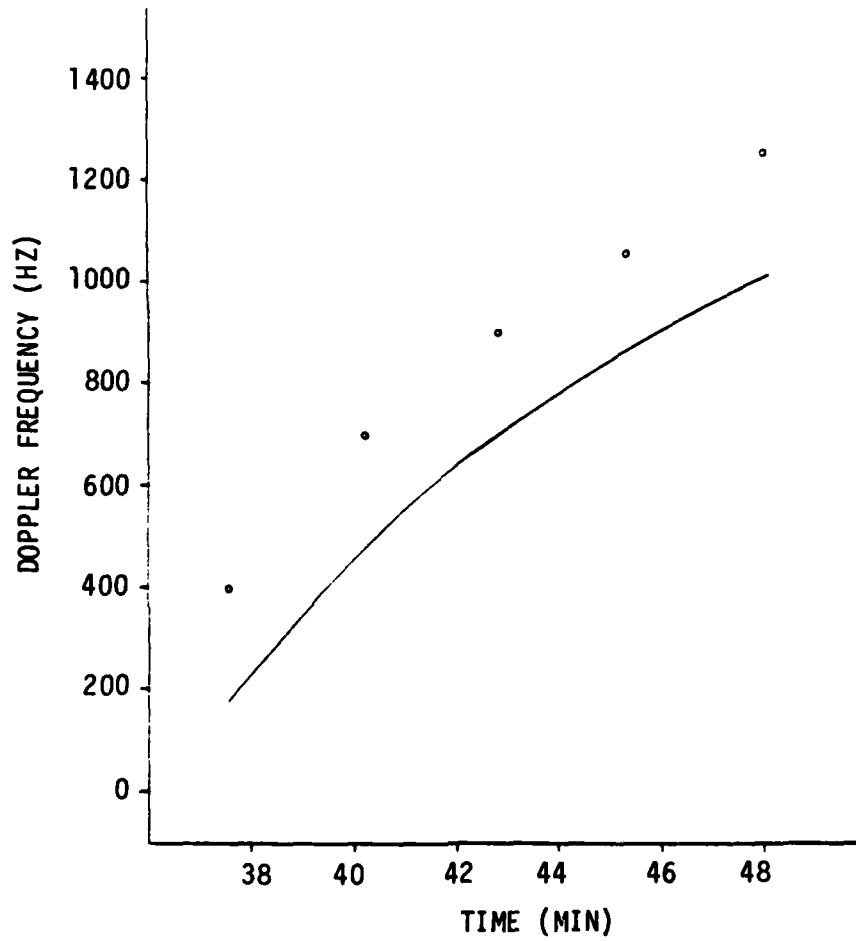
Figure A-12.   Calculated Doppler Shifts (Solid Line)
              Due to Earth Rotation and Spacecraft
              Attitude Changes, and Observed Peak
              Frequencies (Circles) for Seasat Rev.
              757

introduced during the transmission and recording of the data which are not accounted for in these calculations.

A.3 RADIOMETRIC EFFECTS

The effects of changes in the Doppler frequency on the radiometric calibration of the data depend on how the data are processed. Normally, an aperture is placed in the frequency plane of the processor to block out the alias spectrum, in order to avoid azimuth ambiguities in the image. If this is done, the effective gain of the system will vary significantly along the swath, even if the location of the aperture is moved so as to track the changes in the spectrum location. This effective gain, defined as the ratio of the output power to the input power within the frequency aperture, is plotted versus the peak Doppler frequency in Figure A-13 for an aperture width of 900 Hz centered about the peak frequency. The same gain factor is plotted versus time for Rev. 757 in Figure A-14. It is apparent that this is a very significant effect which should be accounted for if the image intensity, or image film density, is used to infer the radar cross section of the surface over a long swath.

The radiometric effects of Doppler shifts are much less pronounced if measurements are made in the frequency plane of the processor using a wide enough aperture to pass both the primary and one alias spectrum, since a decrease in the amplitude of one peak is accompanied by an increase in the amplitude of the other. Note that this method effectively bypasses the image formation process and thus results in a much lower spatial resolution. There is still a slight variation in the effective gain of the system using this method, as shown in Figures A-15 and A-16, but the variation is small compared to other sources of error.

An alternative to this procedure would be to make explicit corrections for Doppler spectrum variations. This could be done by
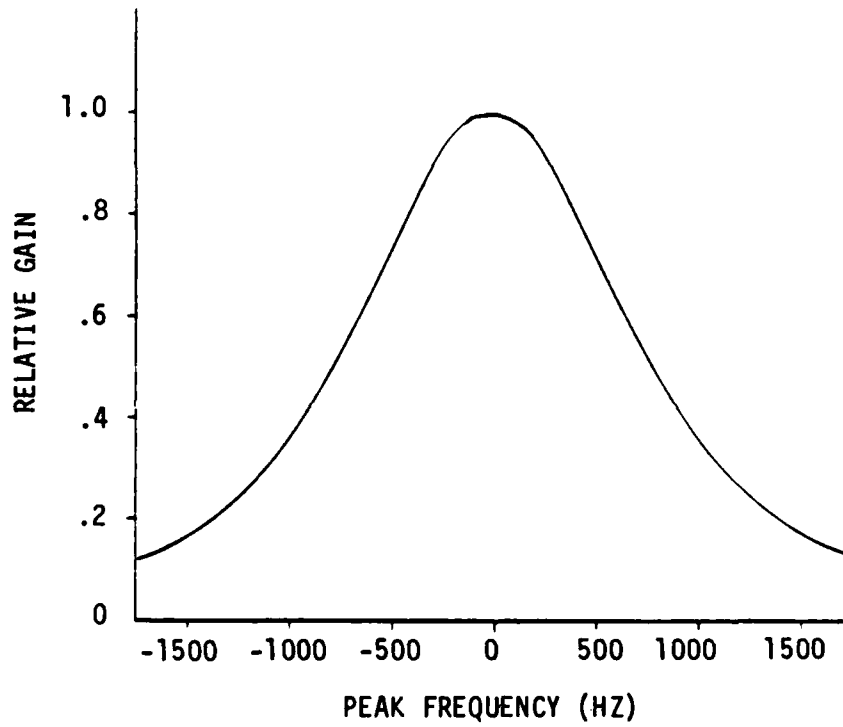
Figure A-13. Ratio of Output-to-Input Power Within a
Frequency Interval of 900 Hz Centered at
the Doppler Peak Frequency
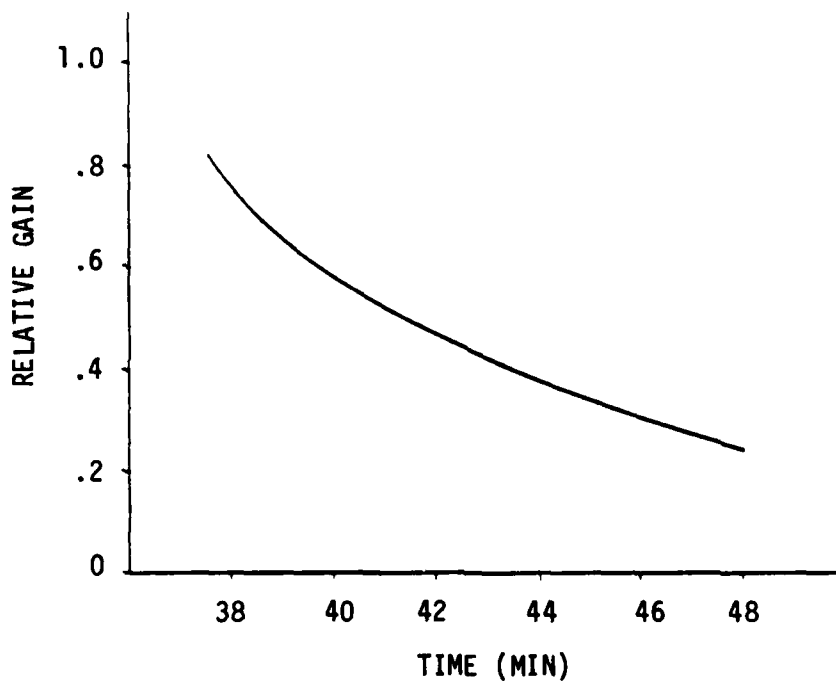
Figure A-14.   Ratio of Output-to-Input Power for a
Segment of Rev. 757, Using a Frequency
Plane Aperture of 900 Hz Width Centered
at the Actual Doppler Peak Frequency
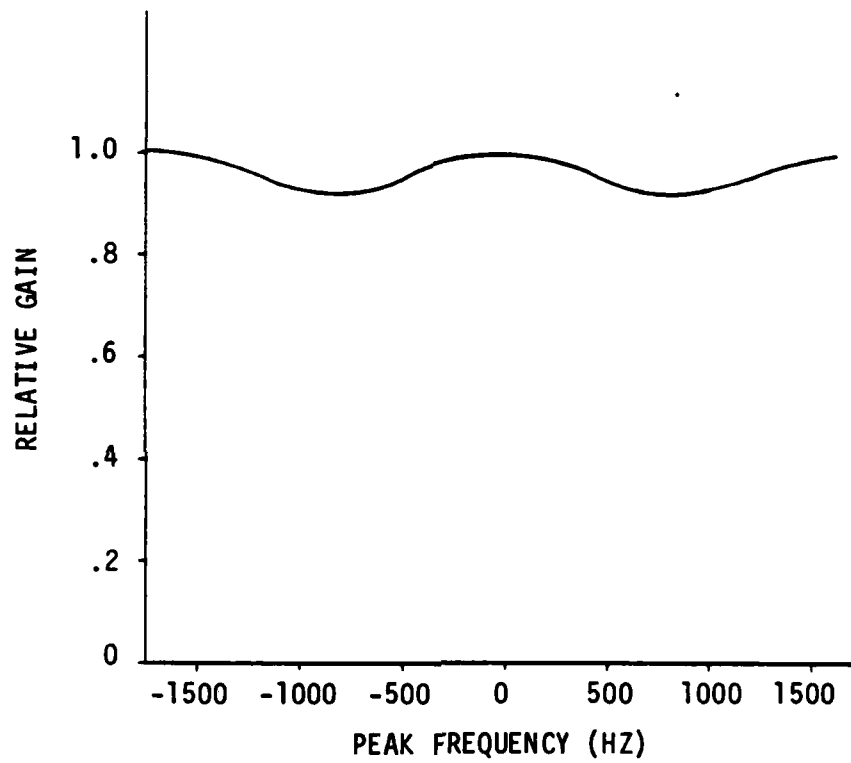
Figure   A-15.   Ratio of Output-to-Input Power for a Frequency Interval from -PRF to +PRF Versus Doppler Peak Frequency
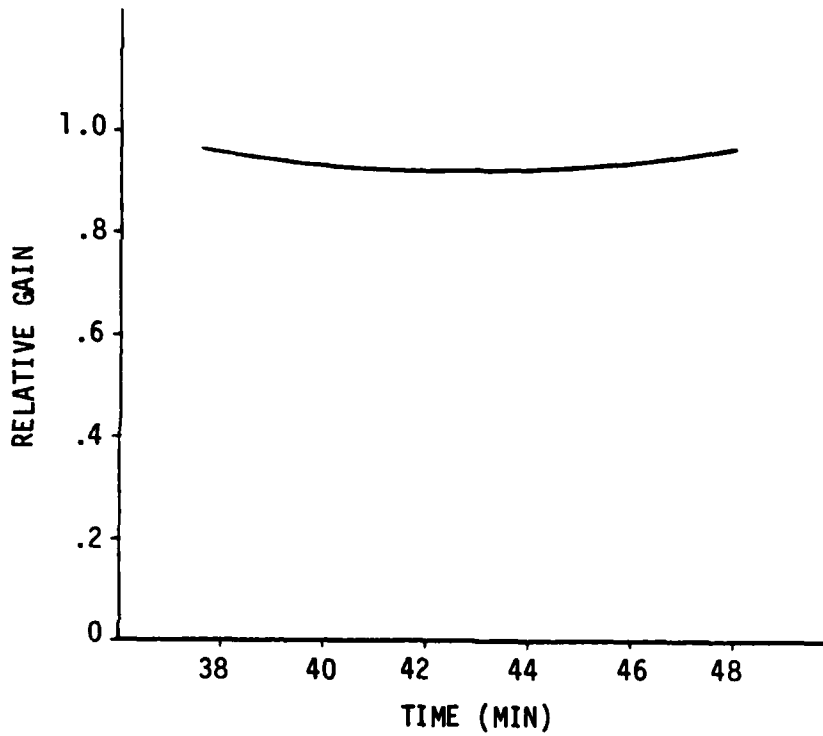
Figure A-16. Ratio of Output-to-Input Power for a
Segment of Rev. 757, Using a Frequency-
Plane Aperture From -PRF to +PRF

measuring the peak Doppler frequency at several points along the pass and calculating the gain as was done here. Such a correction would be especially important for measurements made on conventionally processed image films over large swath lengths.

A.4 SUMMARY

Using optical processing techniques, variations in the Doppler spectrum of the received signal are observed to significantly affect the radiometric characteristics of Seasat SAR image data. These effects are sufficiently important that they should be accounted for if the image intensity is to be used to infer radar cross section over a long image swath, as, for example, in the measurement of surface wind speeds. It is found that these effects are much less pronounced if measurements are made in the frequency plane of the processor using an aperture which is wide enough to pass both the primary and one alias spectrum. These effects can also be corrected by determining a calibration curve of the effective gain for the pass from measurements of the peak Doppler frequency as a function of time. This correction method is especially applicable to intensity measurement made on conventionally processed image films over large swath lengths. Determination of a proper MTF is important in the latter correction method, but is not needed in the frequency plane method.

REFERENCES

Allan, T.D. and T.H. Guymer, Seasat and JASIN, Int. J. Remote Sensing, 1, pp. 261-267, 1980.

Anonymous, Seasat-JASIN Workshop, Pasadena, CA, 18-26 March, 1980.

Beal, R.C., The Seasat SAR Wind and Ocean Wave Monitoring Capabilities: A Case Study for Pass 1339M, 28 September 1978, Johns Hopkins University/Applied Physics Laboratory Report No. SIR 79 U-019, 1979.

Beal, R.C., P.S. DeLeonibus, and I. Katz (eds), Spaceborne Synthetic Aperture Radar for Oceanography, Johns Hopkins Univ. Press, Baltimore, MD, 215 pp., 1981.

Brown, W.M. and L. Porcello, An Introduction to Synthetic Aperture Radar, IEEE Spectrum, 6, pp. 52-66, 1969.

Cox, C.S. and W. Munk, Statistics of the Sea Surface Derived from Sun Glitter, J. Mar. Res., 13, pp. 198-227, 1954.

Daley, J.C., Wind Dependence of Radar Sea Return, J. Geophys. Res., 78, pp. 7823-7833, 1973.

Gloersen, P., and F.T. Barath, A Scanning Multichannel Microwave Radiometer for Nimbus-G and Seasat-A, IEEE J. of Oceanic Eng., OE-2, pp. 172-178, 1977.

Harger, R.O., Synthetic Aperture Radar Systems, Academic Press, New York, NY, 240 pp., 1970.

Huneycutt, B.L. Amplitude Calibration for Seasat-A Optically Processed Data, JPL Interoffice Memorandum 334.5-106, July 1979.

Jones, W.L., L.C. Schroeder, and J.L. Mitchell, Aircraft Measurements of the Microwave Scattering Signature of the Ocean, IEEE J. of Oceanic Eng., OE-2, pp. 52-61, 1977.

Jones, W.L., V.E. Delnore, and E.M. Bracalente, The Study of Mesoscale Ocean Winds, in Spaceborne Synthetic Aperture Radar for Oceanography, ed. by R.C. Beal, P.S. DeLeonibus, and I. Katz, Johns Hopkins Univ. Press, Baltimore, MD, pp. 87-94, 1981.

Jones, W.L., P.G. Black, D.M. Boggs, E.M. Bracalente, R.A. Brown, G. Dome, J.A. Ernst, I.M. Halberstan, J.E. Overland, S. Petehuerych, W.J. Pierson, F.J. Wentz, P.M. Woiceshyn, and M.G. Wurtele, Seasat Scatterometer: Results of the Gulf of Alasks Workshop, Science, 204, pp. 1413-1415, 1979.

Jones, W.L. and L.C. Schroeder, Radar Backscatter from the Ocean: Dependence on Surface Friction Velocity, Boundary-Layer Meteorol., 13, pp. 133-149, 1978.

Jordan, R.L., The Seasat-A Synthetic Aperture Radar System, IEEE J. of Oceanic Eng., OE-5, pp. 154-164, 1980.

Kozma, A., E.N. Leith, and N.G. Massey, Tilted-Plane Optical Processor, Applied Optics, 11, pp. 1766-1777, 1972.

Longuet-Higgins, M.S., On the Skewness of Sea-Surface Slopes, J. of Phys. Oceanogr., 12, pp. 1283-1291, 1982.

Lyzenga, D.R., A.L. Maffett, and R.A. Shuchman, The Contribution of Wedge Scattering to the Radar Cross Section of the Ocean Surface, IEEE Trans. on Geoscience and Remote Sensing, GE-21, pp. 502-505, 1983.

Lyzenga, D.R., A. Klooster, J. Marks, and R.A. Shuchman, Evaluation of ERIM Optically Processed Data, ERIM Informal Information Report No. 157800-1-F, Ann Arbor, MI, 41 pp., 1982.

Pravdo, S.H., B. Huneycutt, B.M. Holt, and D.N. Held, Seasat Synthetic-Aperture Radar Data User's Manual, JPL Publication 82-90, 1983.

Shuchman, R.A., A.L. Maffett, and A. Klooster, Static Modeling of a SAR Imaged Ocean Scene, IEEE J. Oceanic Eng., OE-6, pp. 41-49, 1981.

Thompson, T.W., D.E. Weissman, and F.I. Gonzalez, Seasat SAR Cross-Section Modulation by Surface Winds: GOASEX Observations, Geophys. Res. Ltrs., 8, pp. 159-162, 1981.

Valenzuela, G.R., Theories for the Interaction of Electromagnetic and Oceanic Waves - A Review, Boundary-Layer Metoerology, 13, pp. 61-85, 1978.

Wright, J.W., Backscattering from Capillary Waves with Application to Sea Clutter, IEEE Trans. Antenna Propagat., AP-14, pp. 749-754, 1966.

Wright, J.W., A New Model for Sea Clutter, IEEE Trans. Antenna Propagat., AP-16, pp. 195-223, 1968.

Wu, C., B. Barkan, B. Huneycutt, C. Leang, and S. Pang, An Introduction to the Interim Digital SAR Processor and the Characteristics of the Associated Seasat SAR Imagery, JPL Publication 80-26, 1981.

END

FILMED

4-84

DTIC